A SEARCH
FOR COSMIC
GAMMA RADIATION

D. R. HEARN

GPO PRICE $ _____

CFSTI PRICE(S) $ _____

Hard copy (HC) _____ *3.00* _____
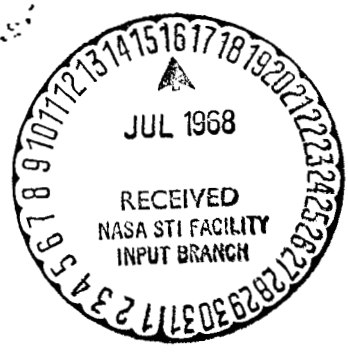
Microfiche (MF) _____ *.65* _____

ff 653 July 65

N 68 - 29434

JUL 1968

RECEIVED
NASA STI FACILITY
INPUT BRANCH

Smithsonian Astrophysical Observatory
SPECIAL REPORT 277

A SEARCH FOR CELESTIAL SOURCES OF GAMMA RAYS
OF ENERGY GREATER THAN 100 MEV

David R. Hearn

Presented as a thesis
to the Department of Physics,
Harvard University

May 17, 1968

804-96

TABLE OF CONTENTS

LIST OF ILLUSTRATIONS

LIST OF ILLUSTRATIONS (Cont.)

LIST OF TABLES

ABSTRACT

A gamma-ray detector consisting of scintillation counters and a spark chamber to convert gamma rays to electron-positron pairs was flown with a balloon to an altitude of 125,000 feet for 7 hours on 28 May 1966. The image of the resulting charged-particle tracks in the spark chamber was transmitted from a vidicon television camera in the balloon gondola to a ground receiving station, where it was recorded on video tape and movie film in real time. The direction of each gamma ray recorded was reconstructed in celestial coordinates. No definite celestial sources of gamma rays were found. Using the integrated-liklihood method, we find 95% confidence flux upper limits of 8.7×10^{-5} $(cm^2 \ sec)^{-1}$ from the Crab Nebula, 9.4×10^{-5} $(cm^2 \ sec)^{-1}$ from the sun, and 2.7×10^{-4} $(cm^2 \ sec \ sr)^{-1}$ from the anticenter of the Galaxy, for photon energies above 100 MeV. Some possible evidence for gamma rays emitted during solar flares is given. The photon spectrum at 4 g cm^{-2} atmospheric depth is reported. The angular resolution of the detector and method of determining statistical upper limits of fluxes are thoroughly discussed.

RÉSUMÉ

Le 28 mai 1966, nous avons fait voler sur un ballon, pendant 7 heures, à une altitude de 125.000 pieds, un détecteur de rayons gamma, comprenant des compteurs de scintillation et une chambre à étincelle, qui transformait les rayons gamma en paires électron-positron. L'image des traces des particules chargées résultantes, obtenus dans la chambre à étincelle, était transmise à partir d'une caméra de télévision à tubes vidicon, mise dans la nacelle du ballon, à une station réceptrice au sol, où elle était instantanément enregistrée sur une bande video et un film. La direction de chaque rayon gamma était reconstituée en ordonnées célestes. Nous n'avons pas trouvé de sources célestes précises de rayons gamma. En employant la méthode de vraisemblance intégrée, nous trouvons avec une certitude de 95%, des limites supérieures du flux de $8,7 \times 10^{-5}$ $(cm^2 \; sec)^{-1}$ en provenance de la Nébuleuse du Crabe, de $9,4 \times 10^{-5}$ $(cm^2 \; sec)^{-1}$ en provenance du soleil, de $2,7 \times 10^{-4}$ $(cm^2 \; sec \; sr)^{-1}$ en provenance de l'anticentre de notre galaxie, ceci pour des énergies de photons supérieures à 100 MeV. Nous donnons certaines preuves d'une émission de rayons gamma pendant les éruptions solaires. Nous montrons le spectre de photons à une profondeur atmosphérique de 4 g cm^{-2}. Nous discutons en détails de la résolution angulaire du détecteur et de la méthode de détermination des limites supérieures statistiques des flux.

КОНСПЕКТ

$28^{го}$ мая 1966 года детектор гамма-лучей состоящий из счет-
чиков мерцаний и камеры со вспышкой для превращения гамма-лучей
в электрон-позитрон пары, летал с воздушным шаром на высоте в
125.000 футов в течение 7 часов. Изображение траекторий заряжен-
ных частиц в камере со вспышкой передавалось из видикон телеви-
зионной камеры находящейся в гондоле шара на станцию на земле где
оно немедленно было записываемо на видеоленту и кинопленку.
Направление каждого записанного гамма-луча было восстановленно
в небесных координатах. Не было найдено определенных небесных
источников гамма-лучей. Употребляя метод сгрупированных правдо-
подобий, мы находим 95% верхний доверительный предел потока в
$8,7 \times 10^{-5}$ (см^2 сек)$^{-1}$ для Крабовидной туманности, $9,4 \times 10^{-5}$(см^2
сек)$^{-1}$ для солнца и $2,7 \times 10^{-4}$ (см^2 сек sr)$^{-1}$ от антицентра Гала-
ктики для фотоновых энергий превышающих 100 Мэв. Приводится неко-
торая возможная очевидность излучения гамма-лучей во время солнеч-
ных вспышек. Докладывается о спектре фотонов на атмосферной глу-
бине в 4 г см$^{-2}$. Приводится тщательное обсуждение угловой разре-
шающей способности детектора и метода определения статистических
пределов потоков.

A SEARCH FOR CELESTIAL SOURCES OF GAMMA RAYS
OF ENERGY GREATER THAN 100 MEV

David Hearn

1. INTRODUCTION

In recent years, many new windows on the universe have been opened
by studying the radiations received in widely divergent bands of the electro-
magnetic spectrum. This paper describes an experimental search for
extraterrestrial objects emitting gamma rays of energies between 50 MeV
and 2000 MeV, carried out with a spark chamber telescope flown from a
balloon. A large body of literature on gamma-ray astronomy, both theoret-
ical and experimental, has been reviewed to January 1967, by Giovanni G.
Fazio (Fazio, 1967). That review also covers a wider energy range than
this paper, and diffuse cosmic gamma-ray fluxes, which are not considered
here. More recent papers will be found in the Proceedings of the Tenth
International Conference on Cosmic Rays (Calgary Proceedings, 1967).

Although no definite evidence for cosmic gamma-ray fluxes has been
found as of April 1968, there are many reasons to expect measurable fluxes
to exist. Observations made of radio, optical, and x-ray fluxes from celes-
tial objects are used to formulate models of the nature of those objects. The
models yield predicted gamma-ray fluxes at the earth. Measurement of a
gamma-ray flux in turn would lead to refined values of the magnetic fields,
optical photon densities, gas densities, and high-energy particle spectra in
the models. Even upper limits to gamma fluxes can eliminate some physical
models.

There are three principal mechanisms for production of gamma rays of
> 100 MeV energy. The first two require high-energy electrons, which are
thought to be responsible for the cosmic radio emission at lower frequencies.

1

High-energy nuclear particles, such as the primary cosmic rays, are needed for the other (see Rossi (1952)).

A. A high-energy electron, colliding with a photon, usually transfers most of its energy to the photon, which is then a gamma-ray photon. This is called inverse Compton scattering. A starlight photon, of energy $\sim$ 1eV, becomes a 100 MeV gamma ray when struck by an electron of $\sim$ 5 GeV.

B. When the electron produces a real photon by colliding with a virtual photon of the electromagnetic field of another charged particle, the process is called Bremsstrahlung. It is the same electrodynamic process as A. In this case, the photon produced has about the same energy as the incident electron.

C. Gamma rays are also produced in the electromagnetic decay of strongly interacting particles, such as π^{o} mesons and certain hyperons. These decaying particles are produced in collisions of nuclear particles, such as protons, with other nuclei. The decay photons have energies on the order of 1/2 the total energy of the decaying particle.

For any given production mechanism $\underline{m}$, the intensity of gamma rays of energy E_γ reaching the earth from a given direction may be calculated from equation (1):

$$I_\gamma(E_\gamma)dE_\gamma = \int_0^\infty \int_{E_\gamma}^\infty N_T(r)\sigma_{\underline{m}}(E_p, E_\gamma)I_p(r, E_p)\, dE_p\, dr \quad . \tag{1}$$

In equation (1), $I_p(r, E_p)$ is the (assumed isotropic) intensity of energetic photon-producing particles of energy E_p at distance r, $\sigma_{\underline{m}}(E_p, E_\gamma)$ is the differential cross section for production of a photon of energy E_γ by mechanism $\underline{m}$, and $N_T(r)$ is the density of target particles at r. Gamma-ray absorption by the interstellar medium may be neglected at the energies

considered here. In the case of a localized region producing gamma photons, the distance integration in equation (1) is confined to the thickness of the source region. An integration over the solid angle subtended by the region then yields the flux (photons per unit area per unit time) from that source.

Obviously, any prediction of gamma-ray flux from a given source is only as good as the numbers used, which are known only indirectly from optical, radio, and x-ray data. Some integral fluxes of photons above 100 MeV energy calculated for the more promising objects are indicated in Table 1 (Fazio, 1967). The best understood object is the remnant of the supernova of 1054 A.D., known as the Crab Nebula. The observed and predicted electromagnetic spectrum of the Crab Nebula is shown in Figure 1. Measurements or upper limits of gamma-ray fluxes will yield better values for high-energy particle intensities, and gas and optical photon densities in distant regions of space. Together with radio flux data, gamma-ray fluxes will provide better values of magnetic field strengths in distant objects.

Table 1. Theoretical fluxes of gamma rays above 100 MeV energy from discrete celestial sources.

Object	Flux $(cm^2 \ sec)^{-1}$		
	high	typical	low
Taurus A (Crab Nebula)	10^{-4}	4×10^{-6}	5×10^{-9}
Cygnus A	10^{-4}	2×10^{-7}	10^{-8}
Virgo A (M87)		9×10^{-9}	
Centaurus A		4.3×10^{-8}	
Sagittarius A		10^{-4}	
Andromeda Nebula (M31)		10^{-7}	
3C273B		5×10^{-6}	
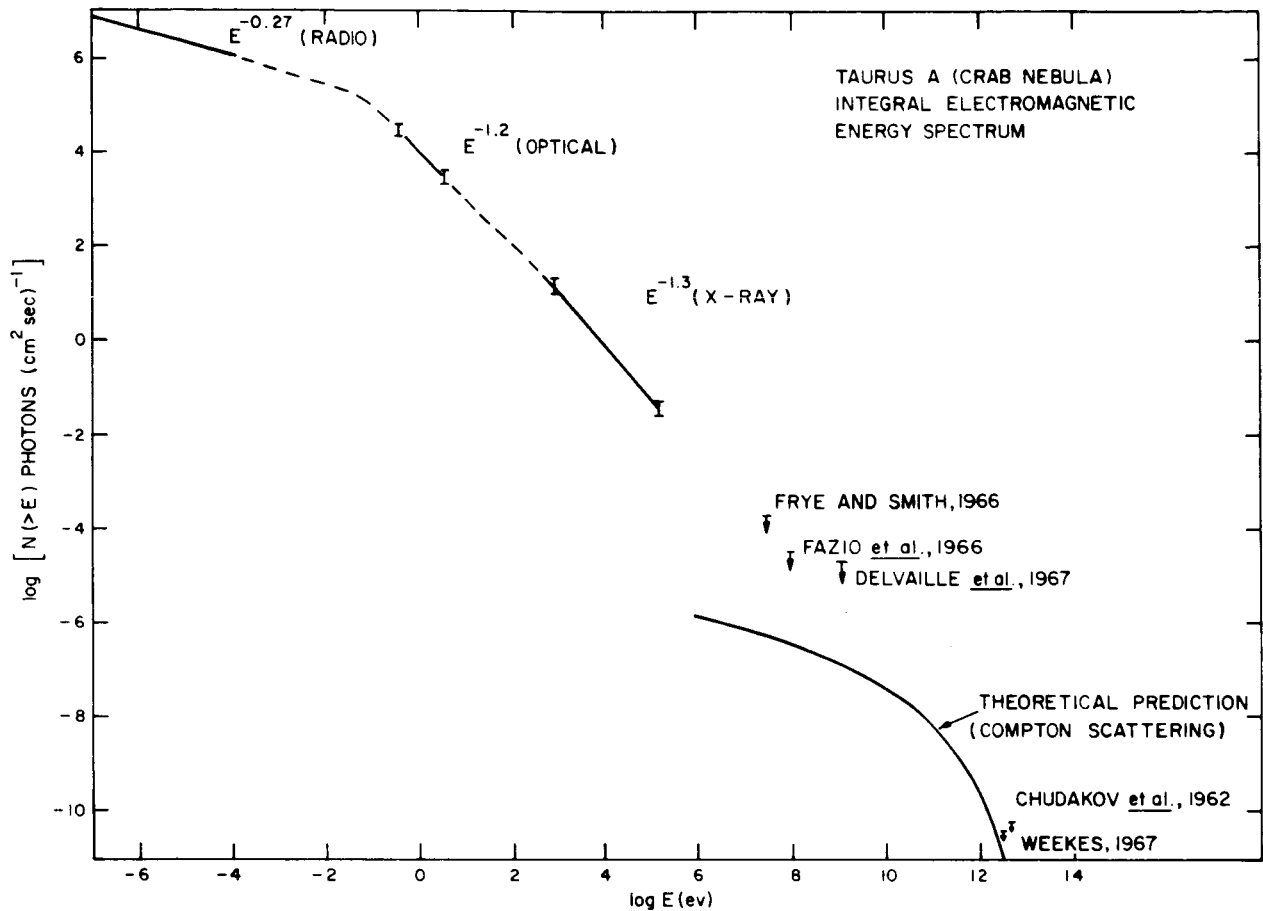
Figure 1. Integral electromagnetic energy spectrum of the Crab Nebula.

In addition to objects that are suspected of emitting gamma rays because they emit radio and x-radiation, there may be other classes of objects radiating gamma photons. If cosmic rays are accelerated in small regions of space, gamma rays should also be coming from those locations. In sum, any direct observation of cosmic gamma radiation will have great, but not easily predicted consequences for astrophysical theory.

Attempts to measure fluxes of cosmic gamma rays must overcome two problems presented by the atmosphere of the earth. First, the attenuation length of these photons is ~ 50 g cm^{-2}, compared with the total atmospheric thickness of 1000 g cm^{-2}. Second, cosmic rays striking the atmosphere produce a strong background of gamma rays, largely from the decay of π^{o} mesons. Thus a gamma detector must be used above as much of the atmosphere as possible. A satellite orbit is the best place. A sub-orbital rocket flight however, does not provide enough time to collect counts with a detector of manageable size. The simplest practical vehicle for a gamma detector is a high-altitude balloon. It can hold the detector at 2 to 10 g cm^{-2} atmospheric depth for up to 10 hours, depending on the winds and the weight of the detector. Balloon-borne experiments will be the only ones considered here.

A balloon-borne experiment has little hope of finding any predicted diffuse or isotropic intensities of photons above 50 MeV, since atmospheric background is several times larger than these general cosmic intensities. One can profitably look for fluxes from specific directions. This requires a detector with the ability to reveal the direction of the photon with reasonable precision. The background then becomes that part of the atmospheric intensity subtended by the detector's cone of angular resolution. The problem is to keep the resolution cone small and accumulate as many counts as possible for statistical accuracy.

The direction-resolving gamma-ray detectors used so far utilize the pair-production process to detect the photon and reveal its direction. In this process, a gamma ray entering the strong electric field of an atomic nucleus materializes into an electron-positron pair, which emerges with almost the same total energy and momentum as the incident photon. A small recoil momentum given to the nucleus allows the process to conserve momentum and energy. The cross-section for the process rises at first logarithmically with photon energy from 1.02 MeV, but reaches a limiting value at high energy due to screening of the nuclear electric field by atomic electrons. The trails of ionization left by the pair of charged particles allow the event to be detected and the particle directions measured.

The factors which limit the energy threshold of practical detectors are the range and multiple scattering of the pair-produced electrons. (Hereinafter the term electron will be used for both positive and negative electrons.) The short range and severe multiple scattering of electrons below 5 or 10 MeV make it difficult simultaneously to detect the electrons and reveal their directions with precision. Detectors with angular resolution good enough for use with balloons generally have effective energy thresholds of 50 to 100 MeV.

Until 1968, the spark chamber has been the preferred device for revealing the directions of the electron tracks. It is sometimes used to isolate the position and time of occurrence of pair-production events in nuclear emulsions. More often, the pair production is intended to occur within the chamber structure. The electrons traverse scintillation and/or Čerenkov counters, and the resulting pulses produce a spark chamber triggering pulse by way of logic circuitry. The trigger pulse is amplified and breaks down a spark gap, which results in the application of a high voltage ($\sim$ 10 KV) to alternate parallel plates of the spark chamber. Sparks form along the trails of ionization left in the gas $\sim$ 1/4 μsec earlier by the electrons passing through the plates. Thus the particle tracks are made accessible to recording and measurement. This method allows inspection of the tracks to verify that it was a pair-production event that triggered the spark chamber. Also, the charged particle backgrounds may be rejected by other counters placed in anticoincidence above or around the spark chamber.

Many methods exist for recording the locations and sometimes intensities of the sparks in the spark chamber. The simplest is to photograph the chamber. This has the drawback that large quantities of film must be carried with the detector for a reasonable number of events. Also, it is a major task to analyze the resulting film. A similar method employs a television camera to view the chamber. Here the filming can be done on the ground. Furthermore, this method lends itself to automatic electronic analysis of the spark locations. Two methods that also allow or even require electronic analysis are the wire spark chamber and the acoustic spark chamber. In

the wire chamber, the spark jumps to a wire among a plane of parallel wires, instead of to a solid plate. The spark is then located in one direction by which wire carries the current pulse of the spark. A second plane of wires gives the other coordinate value. This method is ideally suited to digital data transmission. In the acoustic spark chamber, the spark is located in space by the time of arrival of its sound at two or more microphones in the chamber.

The photographic spark chamber can most easily be made to give good resolution of the spark positions. A high rate of false triggerings, however, will soon limit the number of useful gamma-ray events that can be obtained in one flight. The wire and acoustic spark chambers become complicated when more than one track must be located, as in the case of pair-production events. In addition, it has generally been necessary to examine each event visually to reject complicated background events, which occur frequently. For the present, the television system, or vidicon spark chamber, is a very suitable device for conducting general searches for celestial sources of gamma rays from balloon altitudes.

Some typical results of cosmic gamma-ray experiments are given in Table 2, adapted from Fazio (1967). More recent data are to be published (Calgary proceedings, 1967). Some of the upper limits quoted may be too low, due to erroneous methods of treating the statistical data. For example, the results originally published for this experiment (Fazio, Helmken, Cavrak, and Hearn, 1967), using the statistical method accepted at the time, were too low by as much as a factor of 2. With current balloon technology allowing a detector package of several hundred pounds to be flown for 8 to 10 hours under several grams per square centimeter of overlying atmosphere, the experiments seem to be approaching a smallest upper limit of gamma-ray source fluxes above 100 MeV of 10^{-5} $(cm^2 \ sec)^{-1}$. At higher threshold energies, the limits can be set lower due to lower backgrounds, but all of the predicted source spectra are lower also. In order to improve significantly on this performance in the future, balloon experiments must employ much larger detectors.

Table 2. Experimental upper limits to gamma-ray fluxes
from discrete sources.

Object	Energy threshold (MeV)	Flux limit $(cm^2\ sec)^{-1}$
Taurus A (Crab Nebula)	100	7×10^{-5}
Cygnus A	100	5×10^{-4}
	10^3	6×10^{-4}
Cassiopeia A	100	2.3×10^{-3}
	10^3	2.9×10^{-4}
Virgo A (M87)	100	2.7×10^{-4}
Andromeda Nebula	100	1.6×10^{-3}
	10^3	1.5×10^{-4}
Sun (quiet)	50	10^{-3}
	100	5.3×10^{-3}

Although this experiment has already been reported briefly (Fazio and
Helmken, 1965; Helmken and Fazio, 1967; Fazio, Helmken, Cavrak, and
Hearn, 1967), it is the purpose of the present paper to describe the experi-
ment in detail. Better methods of treating the data have been developed,
and the resulting flux limits have been revised.

The next section describes the actual experiment, up to the reduction of
the data to a set of electron pair directions in celestial coordinates. Section 3
presents the numerical results of this experiment. A discussion of detection
efficiency as a function of energy, and the energy measurements possible
with this detector are included. The observed background intensity at alti-
tude is reported. Upper limits of gamma-ray fluxes from the Crab Nebula,
the sun, and the Galaxy, obtained by the integrated-liklihood method, are
discussed. Evidence for gamma rays possibly emitted by solar flares is
also indicated. Section 4 gives a thorough discussion of the problem of the
angular resolution of this spark chamber experiment.

2. DESCRIPTION OF THE EXPERIMENT

2.1 Flights

Twice the present detector was carried to high altitudes by research balloons. Both balloons were launched by the National Center for Atmospheric Research from the base at Palestine, Texas, 42° North geo-magnetic latitude. NCAR provided position and altitude information throughout each flight. The NCAR telemetry system also allowed control commands to be sent and temperature data to be received from the balloon gondola.

The more recent flight was performed on the night of 10-11 September 1967. The balloon, of 5 million cubic feet volume, held the gondola at a steady altitude of 121,000 feet for 6 hours. The transmitted data were received free of noise out to a range of 300 miles. The failure of a high-voltage power supply at 60,000 feet during ascent severely limited the data from this flight, since no spark chamber tracks were available to identify or reveal the directions of gamma rays converted in the detector at high altitude. Thus only data from the first flight are under consideration here.

The first flight occurred on 28 May 1966. The 5.5 million cubic foot balloon held the gondola at 125,000 feet altitude, corresponding to 4 g cm^{-2} overlying atmosphere, from 1420 to 2020 Universal Time. The trajectory of the balloon ranged from 31° 15' to 31° 40' North latitude, and from 95° 45' to 97° 47' West longitude.

2.2 Apparatus

The apparatus of this experiment comprises three main subsystems. First, the detector itself consists of scintillation and Čerenkov counters, electronic circuitry to recognize desired events, and the spark chamber for revealing the particle tracks. Next, there is the event-recording system,

from the television camera, through the radio transmission link, to the video recorders on the ground. Finally, the pressurized balloon gondola must be supplied with batteries, compass, sun sensors, and miscellaneous recording devices. The heart of the experiment is the spark chamber, acting as an extended gamma-ray converter. It allows a search for gamma sources to be conducted over about 1 steradian of the sky at one time. Detailed properties of the chamber as a photon detector are discussed in Sections 3 and 4.

Although the apparatus has been described briefly elsewhere (Fazio and Helmken, 1965; Helmken and Fazio 1967), a complete description is given here for reference.

A side view of the detector is shown in Figure 2. Counter A is the 1- × 17- × 17-inch plastic scintillation counter in electronic anticoincidence to reject charged particles. It uses two 6199 photomultiplier tubes with separate discriminators. The ratio of cosmic-ray muon tracks accepted by the detector with counter A turned on to that with counter A turned off indicated a rejection efficiency for fast charged particles of > 99.99%. Counters B1 and B2 are both plastic scintillation counters $1/2 \times 5 \times 5$ inches, also using 6199 phototubes.

Counter C is a lead-glass Čerenkov counter, consisting of a block of Schott SF-6FA glass, $18 \times 18 \times 16$ cm (10.2 radiation lengths deep), with a 7819 photomultiplier tube 5 inches in diameter. It serves as a total energy detector. The gain of this counter and the associated pulse-height-analyzer (PHA) circuitry was checked before and after the flight by recording the spectrum produced by cosmic-ray muons traversing B1, B2, and C counters. Those spectra showed also that the pulse-height resolution was 50% (full width at half-maximum divided by most probable pulse height) for those single tracks.
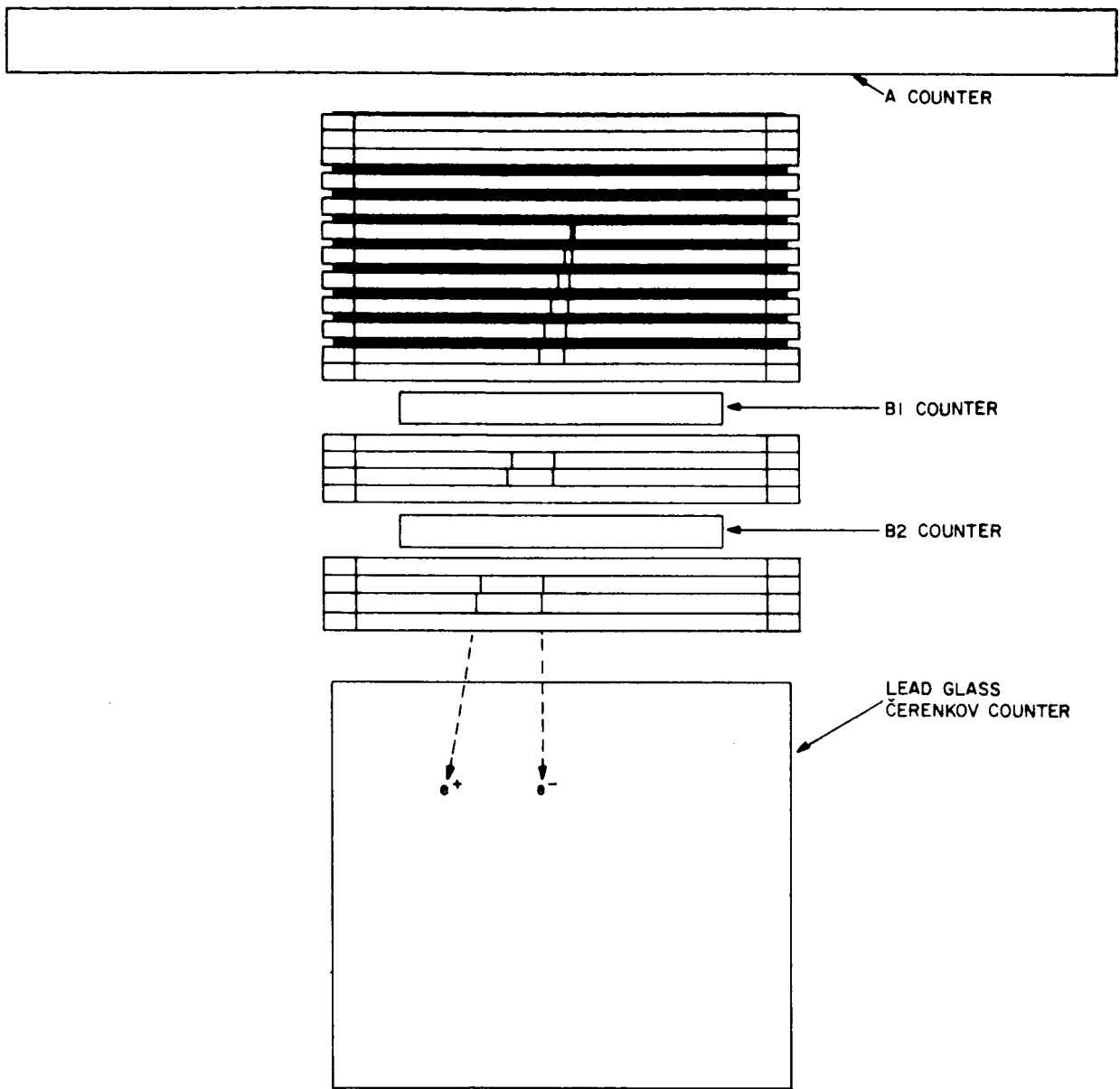
A COUNTER

BI COUNTER

B2 COUNTER

LEAD GLASS
ČERENKOV COUNTER

Figure 2. Diagram of detector. Sparks of hypothetical pair-
production event are shown.

The electronic circuitry is contained in boxes of sheet copper, to avoid the serious radio-frequency interference generated by the firing of the spark chamber. The power for all logic circuitry is regulated to 1%.

Each photomultiplier output goes to a tunnel diode discriminator. The discriminator levels are set to accept ~99% of all minimum-ionizing particles in each counter. The output pulses of the A counter discriminators are 300 to 500 nsec long, while those of the B and C discriminators average 280 nsec. The pulse timings are checked before flight to ensure the proper overlaps.

The normal logical requirement for triggering the spark chamber is $\overline{A}$ B1 B2 C. However, three small relays on the main logic circuit card can be energized by ground command to fire the chamber on $\overline{A}$ B1 B2, B1 B2, or B1 B2 C. These commands were used briefly during the flight to compare the observed count rates with those calculated from known cosmic-ray fluxes.

A signal is derived from the last dynode of the C counter tube and sent to the PHA. There, a pulse-height to time converter and a 200 KHz crystal-controlled clock yield a number of pulses proportional to the input pulse height. The pulses are counted and displayed as a 9-bit binary number by a row of lights near the spark chamber. Other lights in the row are driven from divide-by-eight circuits which count other coincidence pulses, such as B1 B2, B1 B2 C, and $\overline{A}$ B1 B2.

In order to avoid contamination of the gas by electronegative molecules, the spark chamber was built of aluminum plates and glass walls, cemented together with a special epoxy cement, Armstrong A-12 (made by Armstrong Products Co., Inc., Argonne Road, Warsaw, Indiana). The plates are all 7 inches square, and either 0.020 inch (0.0508 cm) or 0.125 inch (0.3175 cm) thick. The walls are built of strips of glass 1/4 inch (0.635 cm) thick and 1/2 inch wide, mitered at the ends. The chamber operates with a commercial mixture of 90% helium and 10% neon sealed in at atmospheric pressure. Even after being sealed in for several months, the gas yields good sparks.

The spark chamber is fired by a spark gap and driver supplied by Science Accessories Corporation. The spark gap is coupled to the chamber by a 0.005-μf capacitor on every other plate. The capacitors are charged to 10 KV through a 10 Megohm resistor by a power supply from Shintron Company of Cambridge. Two hundred nsec elapse between the output pulse of the phototubes and the current rise in the spark chamber. Since no clearing field was used, some fraction of desired events may have been spoiled by lingering ion trails. The system is better than 99.5% efficient in forming sparks along single ion trails. However, when two tracks are present in the same gap, there is only a 50% to 60% probability that both will yield recordable sparks.

The television camera views the spark chamber from two perpendicular directions through a set of mirrors, as diagramed in Figure 3. Plastic field lenses of 55-inch focal length on each side of the chamber provide the camera with a straight-in (orthographic) view of the chamber. Edge-lighted plastic fiducial plates show the limits of the active volume of the chamber. The vidicon television camera, from KinTel division of Cohu Electronics, uses the standard 525 scan lines at 30 frames per second. It is capable of 750 line horizontal resolution, and its geometrical distortion is less than 2% throughout.

Coming from the television camera, the full video signal is amplified and then it frequency-modulates a 1490 MHz transmitter. The horizontal resolution of the system is limited to 350 lines by the transmitted bandwidth of 4 MHz. The transmitter output power is 7.5 watts. A phased-array antenna hanging below the balloon gondola radiates a pancake-shaped pattern with a 6-db lobe 7° below horizontal in all directions.

The signal is received at the mobile tracking station with an 8-foot-diameter parabolic dish antenna. A monitor in the trailer is watched continuously to check system performance and to help in guiding the receiving antenna. To provide a time-reference signal, station WWV is also received in the tracking station through another antenna. Thus we record an audio signal
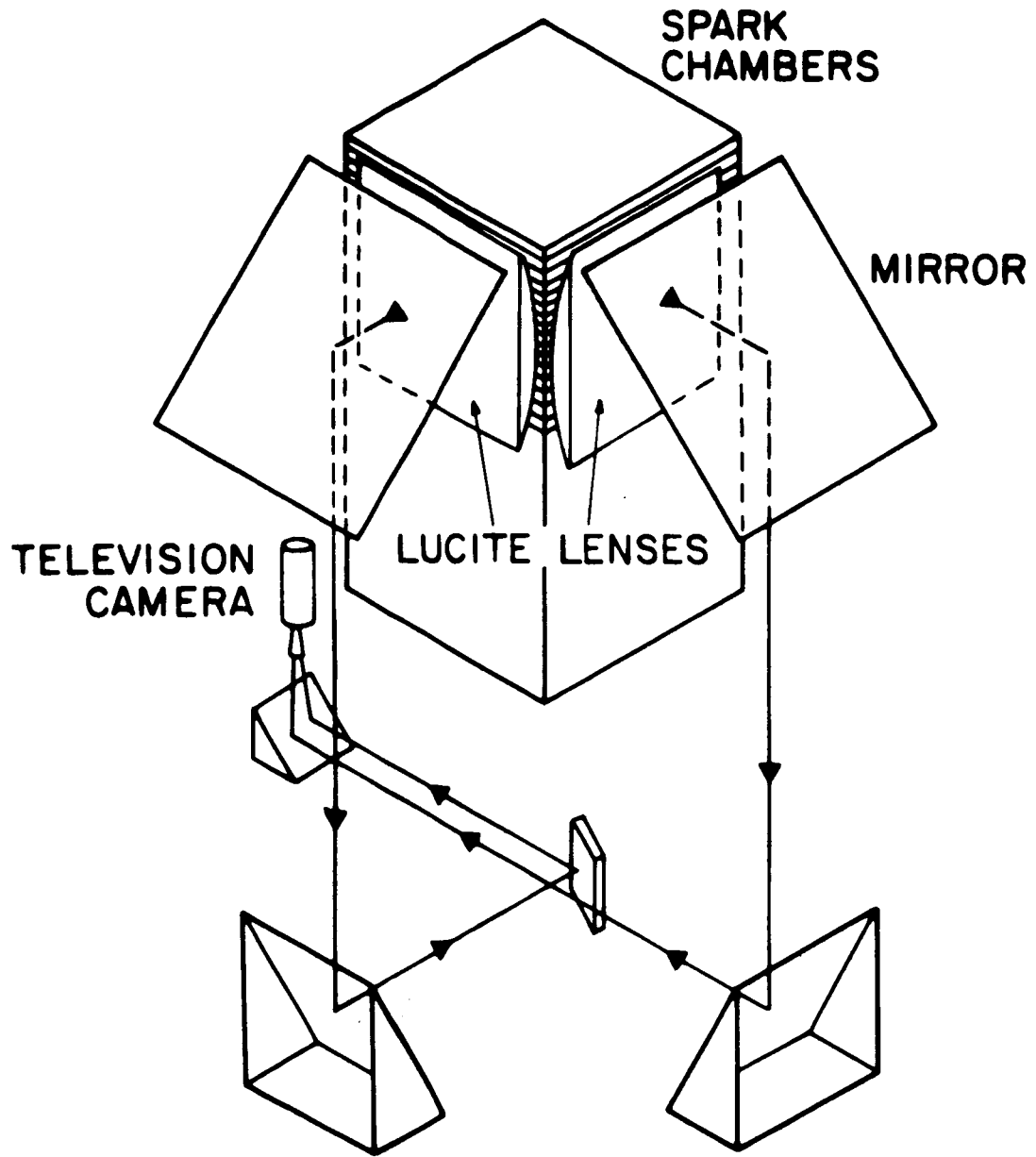
13

Figure 3. Spark chamber optical system (not to scale).

along with the video signal from the gondola. Verbal comments are also put on the audio track, from a microphone.

The primary recording device is a kinerecorder, for photographing a television picture on 16-mm film at the standard rate of 30 frames per second. This was formerly the recording technique used by commercial television networks. The kinerecorder puts the sound track on the film at the same time. It was discovered after the first balloon flight that the kinerecorder image became progressively more distorted during the flight, because the device became very overheated in the confines of the tracking trailer then used.

Though even a time-varying geometric distortion may be taken into account, a second problem posed a more serious limitation. The sparks were so bright that their images on the kinerecorder tube bloomed to excessive widths. On the film, the spark images appeared to be about 1/4 inch wide. Live monitors showed much sharper images, down to 1/16 inch widths.

Several methods are suggested to overcome this problem in the kinerecorder:

A. Decrease the contrast between the spark images and other vital details such as fiducial lines and compass, so that both can be recorded reliably without blooming or oversaturation, by a) decreasing spark energies by using smaller spark chamber driving capacitors, b) blocking some spark light with filters in front of the chamber, or c) increasing the power of the lamps for fiducial lines, etc.

B. Record a negative, rather than positive video picture, so the sparks would show as clear spaces on the film. Overshoot may become a problem, but blooming should be eliminated. This procedure has the added advantage that an event may later be transferred easily to a single frame of another film, even though the spark and data-light images are scattered over several frames of the kinerecorder film. This transfer would reduce the number of frames of film by as much as a factor of 1000. The time information implicit

15

in the original footage number would have to be inserted into the second picture.

In case the kinerecorder should fail during the flight, the audio and video are also recorded on a television tape recorder. The video tape recorder also provides a record of the 15% of the data that are transmitted during kinerecorder film changes. Later, any portion of the video tape can be transferred to film with the kinerecorder. The replayed picture usually has more noise than the original, however.

In searching for discrete sources of gamma rays, the orientation of the detector must be known at all times during the exposure. The gondola suspension turnbuckles are adjusted before flight, to align the axis of the detector to within a small fraction of a degree of vertical. To measure the azimuthal orientation, the television system permits the simple expedient of installing a magnetic compass. This gondola carries a type of compass used in World War II tanks. On the first flight, it could not usually be read to better than 5°, except when the lubber line crossed a 10° mark. For the second flight, a cylinder lens was installed, to show a greater portion of the scale, and permit readings to 1° at any time.

To check the systematic errors of the compass, exact azimuth measurements are obtained from the aspect of the sun. This gondola carries four sun sensors, each consisting of a silicon photovoltaic cell with two rows of bars to create a Moiré pattern shadow on the cell. The solar cells on the four sides are connected in series, and their output is sent through two meter movements in series inside the gondola. One meter is of the projected-light pointer type for display on the television system. The other is in a Rustrak miniature strip-chart recorder. On the first flight, a commutator switch before the meters automatically sampled sun-sensor output along with battery voltages and the output of a logarithmic count-rate meter. Since interruptions in sun-sensor data proved highly undesirable, for the second flight the sun sensors were given a track of their own on the recorder and shown continuously on the lighted meter.

16

When the sun is nearly overhead, the sun sensors do not provide good
azimuth data, due to reflections from the balloon. During morning or after-
noon periods though, very accurate azimuth points are obtained when the
sun-sensor output goes through Moiré minima. These data are used to obtain
an in-flight calibration of the compass which is more accurate than an individ-
ual compass reading.

Silver-zinc batteries are carried in the lower portion of the gondola
next to the transmitter. Most of the power was obtained from a 28 volt
assembly of 40 ampere-hour cells, which proved to have ample capacity for
an 8-hour flight.

Everything but the sun sensors and antenna is contained in the welded
aluminum pressure container, 28 inches in diameter inside, which is in
three sections held together by Marmon clamps and sealed with large O-rings.
A third Marmon clamp holds the 0.014-inch-thick Mylar pressure dome over
the top. This dome had to be bulged slowly by pressure before flight, to
avoid rupture during ascent. The thin Mylar top is necessary to minimize
absorption of primary gamma rays and production of secondaries in front of
the detector. The whole pressure can is covered with polyurethane foam
insulation, which, combined with heat from the transmitter filament, held
the minimum temperature in the gondola to about 10° C during a night flight.
As a precaution against condensation on optical parts, the container was
flushed with dry nitrogen before flight.

For flight, a shorting plug is attached to a 37-pin hermetic connector
in the bottom of the gondola. It carries leads for the sun sensors and relay
leads to the command receiving system provided by the National Center for
Atmospheric Research.

2.3 Data Reduction

The film produced during the flight of 1966 consisted of 15 reels of 1200 feet (about 27 minutes) each. The video tape from that flight proved to result in a very snowy picture when transferred to film on the kine-recorder, and was not adequate for filling the gaps in time between the other 15 reels.

As the first step of analysis, the 1200-foot reels were projected from a standard 16-mm sound projector in order to establish the footage number of each WWV 5-minute time mark. Also, the footage was recorded each time the compass indicated a multiple of $10°$. This was necessary because the compass could easily be read from a moving picture, but not from a stationary frame of film, due to visual noise.

Next, the large reels of film were cut into spools of 100 feet apiece, in order to be studied with 16-mm microfilm readers. The job of searching the film for identifiable events was quite tedious with these simple readers which move the film continuously, since many empty frames moved past for each frame that contained an event. Future scanning will be done with motion picture analyzing projectors which hold the frames steady. The PHA lights were useful when scanning the film backwards in time, since their afterglow was a signal that an event was near.

A method had to be found to compress the data of the identifiable events into a more easily handled form. A simple expedient was found in projecting the event frame onto a sheet of paper with a reference grid printed on it. The film scanner wrote the footage of the event in the appropriate space, and aligned the image of the fiducial lines with the grid. He then marked the location of each spark on the printed line representing the center of each spark chamber gap, and marked the lighted PHA bulbs. Usually the spark and light bulb images were scattered over several frames, and this was a convenient way of seeing the whole event at once, without visual clutter.

In 5 hours and 18 minutes of data analyzed, about 46,000 events were found, of which 505 were considered to be electron-positron pair events originating in the fiducial volume of the chamber, about 7000 were single-track events appearing to originate in the chamber, and the rest either originated outside the fiducial volume, included too many tracks, or had no recognizable structure.

The single tracks appeared to suffer little scattering in the chamber, and had a pulse-height spectrum very similar to that of the pairs. They are probably a background of secondary or tertiary particles arising from the relatively high flux of primary cosmic-ray protons, such as pions or muons decaying at rest in the chamber, or particles originating in the lead glass and stopping in the spark chamber. They showed no directional pattern in celestial coordinates, and will not be considered further here.

The scanners were instructed to consider an event a pair if: a) There were two distinguishable tracks of sparks with a common vertex within the chamber, and b) at least one gap showed one spark from each track. Pair recognition was made more difficult by the great apparent width of the sparks, about 5 mm, and the fact that two sparks formed in one chamber gap with an efficiency of only 56%. The scanner marked the location of the event on the margin of the film with a green felt marker after tracing the event onto a scanning grid sheet.

As the next step, a physicist relocated the event by the green mark, to verify that it could be considered a gamma-ray event. For valid pair events, he added a red mark to the film and drew a line on the sheet which represented a best guess of the direction of each track in each view. The separate views of each track could be put into correspondence by the relative intensities of the sparks in the two tracks.

To begin the spatial reconstruction of the gamma-ray direction, the angle of each track line on the tracing sheet was measured with a protractor. This step was accurate to $1/2°$. Since the television picture had become

19

somewhat compressed vertically, a specially constructed protractor with the same vertical compression was used to give the correct angles directly. The horizontal non-linearity of the picture was not great enough to contribute significantly to track direction errors.

Observation of two small pendulum bobs next to the spark chamber showed that the chamber remained accurately vertical throughout the float phase of the flight. The small bobs truly represent the local vertical though they are hanging in the gondola, hanging in turn from the balloon. This is easily seen from the solution of the double pendulum problem in this case of extremely unequal periods for the normal modes.

Curves of spark chamber azimuth versus time were obtained from the compass readings and the compass calibration curve. Since the parallel bars of the Moiré masks on the sun sensors were 45° from the vertical for the first flight, a graphical computer was constructed to obtain the true azimuth of each sun sensor null from solar elevation and azimuth. The set of calibration points was then fitted with a constant offset and two Fourier harmonics, to produce a calibration curve accurate to 1° or better. The gondola generally required more than 1/2 hour for a complete rotation. The true azimuth was entered on each scanning sheet, using the film footage to fix the time.

The final manual task of event analysis was to punch the information of each event onto computer input cards. Each card contained the time of the event, pulse-height- analyzer reading, true azimuth of the gondola, the projected angle from the vertical of one track in each view, and the gap of origin of the track. Thus there were two cards for each pair event.

Simple computer programs were used to obtain the local azimuth and elevation and the right ascension and declination for each particle track in the spark chamber. An average latitude and longitude were used for the location of the balloon, since they did not vary by more than 1°.

Computer programs were written to use the Smithsonian Astrophysical Observatory's Calcomp incremental digital plotter to draw a Hammer (Aitoff) equal-area projection of the celestial sphere, centered approximately on the point of maximum exposure. The locations of the tracks of each pair were plotted with a line connecting them. The resulting map (see Figure 4) showed no significant clustering of events, apart from that due to the directional response of the detector.

A second way of studying the spatial distribution of the tracks was to sort them into bins of equal solid angle. The resulting matrix of counts again showed no unexpected excess of counts in any direction.

The requirement that a track at a given angle in the chamber originate at a certain spark chamber plate within the fiducial volume, and pass through counters B1, B2, and C to trigger their discriminators, defines an <u>effective area</u> for that plate at that angle. For these plates, of thickness much less than one radiation length, the gamma-ray pair-production probability is proportional to the cosecant of the angle of incidence on the plate. The projection of the effective area perpendicular to the gamma-ray direction is proportional to the sine of this angle, so the detection probability as a function of gamma-ray direction is simply proportional to the effective area in that direction, neglecting electron scattering. The effective area for each track direction has been calculated for each chamber plate and averaged over azimuthal directions, then summed over all converting plates. The result is shown in Figure 5.

Numerical integration of the effective area presented to any point in the sky over the sensitive time of the experiment yields the exposure of that point, commonly denoted AT. The calculation of the <u>exposure</u> of each bin of the celestial sphere into which tracks were sorted allows a calculation of the relative gamma-ray intensity from that direction. On the map of Figure 6, the bins were shaded according to the number of standard deviations by which their calculated intensities differed from the average. No bin showed a significant excess of counts. For Figure 6, electron tracks
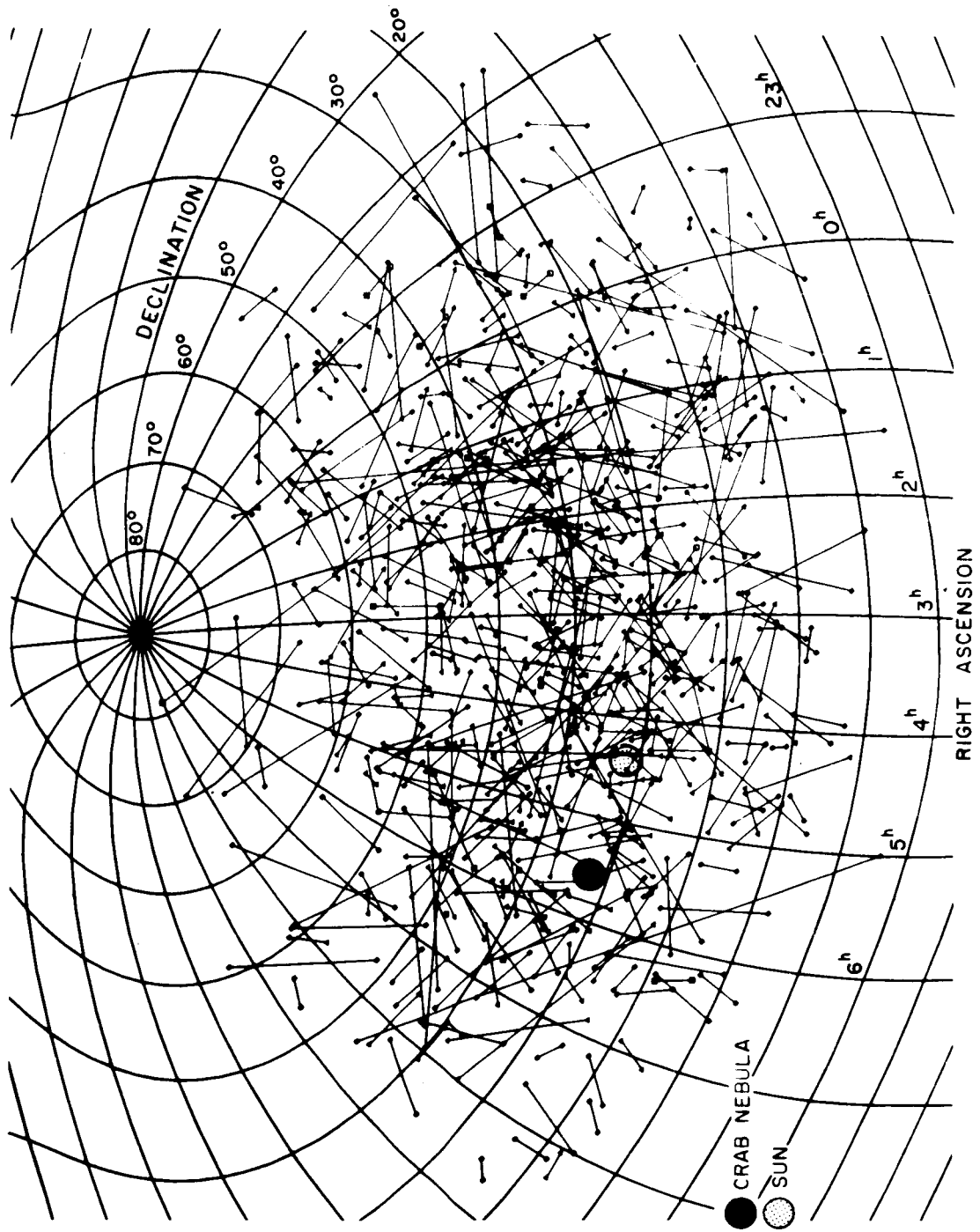
Figure 4. Angular distribution over the celestial sphere of electron-positron tracks resulting from gamma-ray pair production; the corresponding electron-positron tracks are joined by a straight line.
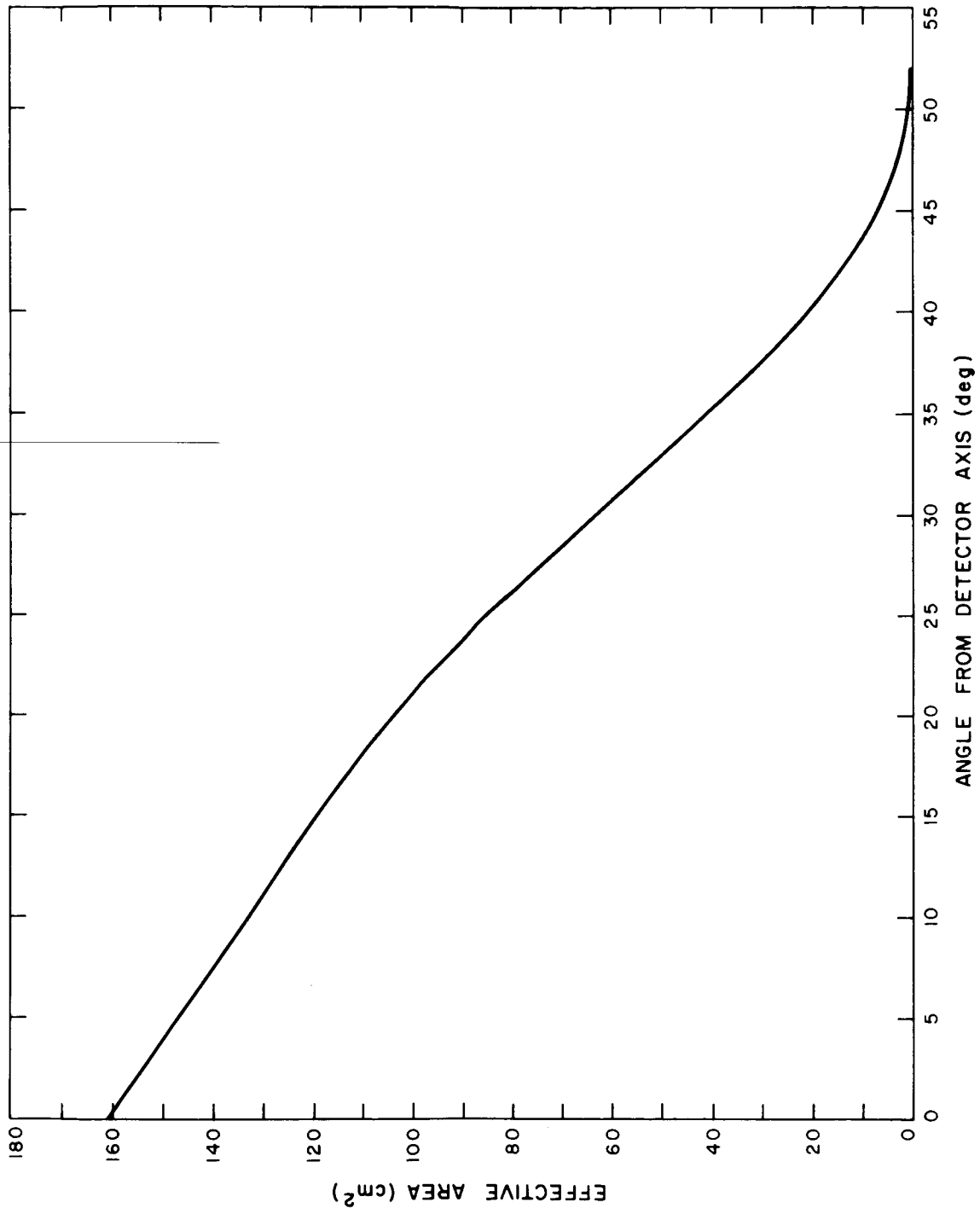
22

Figure 5. Effective area of detector vs. angle.

23
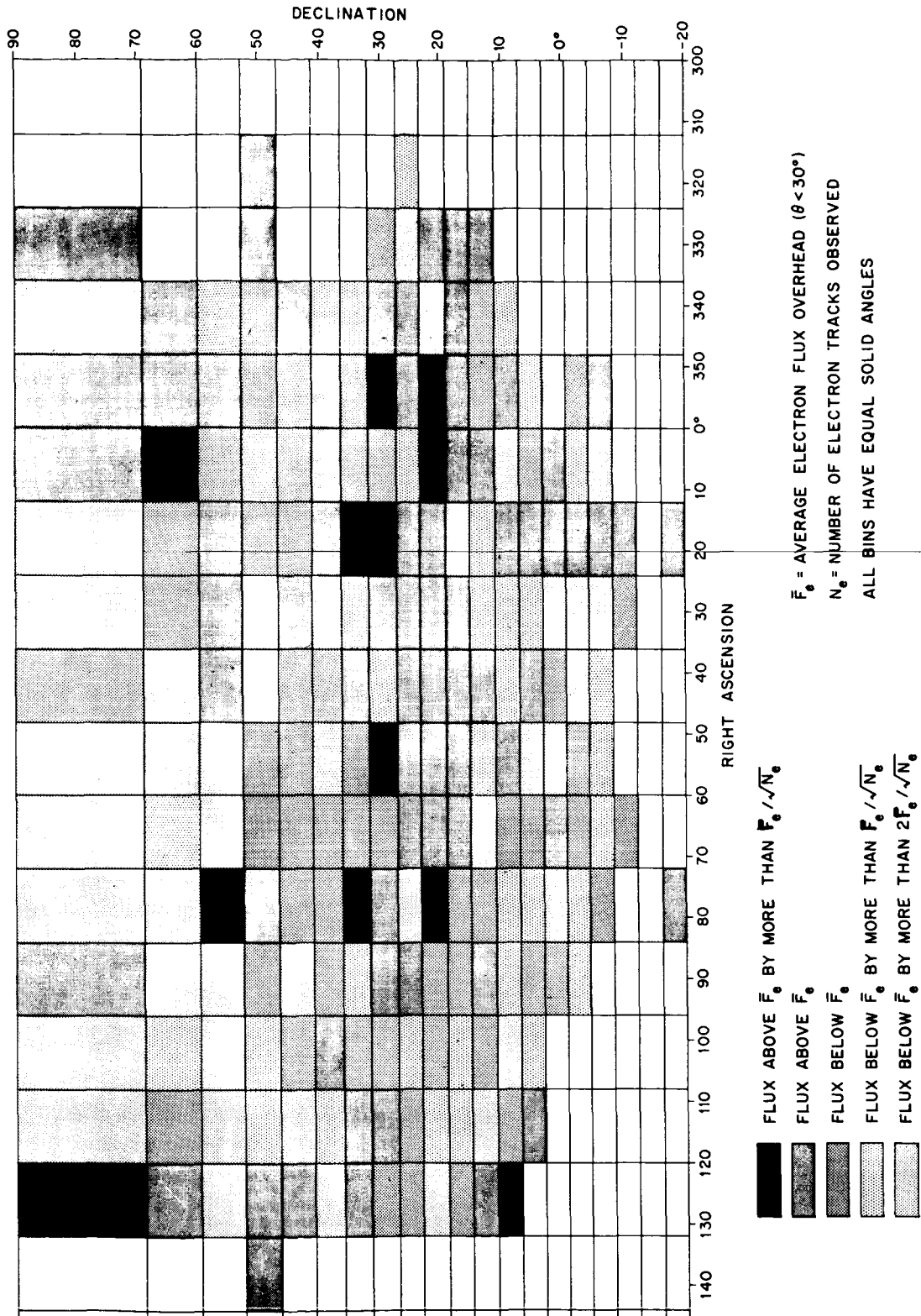
CELESTIAL MAP OF RELATIVE GAMMA RAY FLUXES

$\bar{F}_e$ = AVERAGE ELECTRON FLUX OVERHEAD ($\theta < 30°$)

N_e = NUMBER OF ELECTRON TRACKS OBSERVED

ALL BINS HAVE EQUAL SOLID ANGLES

FLUX ABOVE $\bar{F}_e$ BY MORE THAN $\bar{F}_e / \sqrt{N_e}$

FLUX ABOVE $\bar{F}_e$

FLUX BELOW $\bar{F}_e$

FLUX BELOW $\bar{F}_e$ BY MORE THAN $\bar{F}_e / \sqrt{N_e}$

FLUX BELOW $\bar{F}_e$ BY MORE THAN $2\bar{F}_e / \sqrt{N_e}$

Figure 6. Fluctuations of gamma-ray intensity over the celestial sphere.

24

were used individually to obtain relative intensities. The relative standard deviation of the number of gamma rays would be:

$$\Delta_\gamma / N_\gamma = (2/Ne)^{1/2} \quad ,$$

where Ne is the number of electron tracks in a bin. The conclusion from Figure 6 is that no localized source of gamma rays has been found by this experiment.

3. RESULTS OF THE EXPERIMENT

3.1 Detection Efficiency

For measuring fluxes of any kind, it is vital to know the probability that any given quantum reaching the detector will actually be counted. With gamma rays of hundreds of MeV energy, it is especially difficult to obtain a calibration source of known energy and intensity. For this experiment, a detection probability has been calculated from the pair-production cross-sections, the measured spark formation efficiencies, and the multiple-scattering formulas given by Pinkau (1966a, b, 1968). The calculation neglected particle losses from the edge of the detector, and assumed the gamma rays to be incident parallel to the detector axis. The variations of efficiency with incident direction are contained, to a good approximation, in the expression of effective area.

Certain assumptions had to be made to perform the calculation. For low energies, each electron was required to have more than 10 MeV kinetic energy, in order to make a recognizable track and to trigger the scintillation counters. At high energies, the important requirement was that in at least one gap of the chamber there appear two sparks, separated by more than 0.5 cm so that they would be resolved separately on the kinerecorder film. The numbers assumed here determine rather directly the energies at which the detection efficiency drops to a given fraction of the maximum attainable from the total pair-production cross section.

The result of the calculation is seen in Figure 7, where the total detection probability for all gaps is plotted. The pair-production cross section for aluminum was taken from Evans (1955). (The 5% photon attenuation in the A counter and first three 0.020-inch aluminum plates has been neglected.) At low energies, the differential cross sections in Rossi (1952) were integrated numerically for electron (or positron) energies greater than 10 MeV.
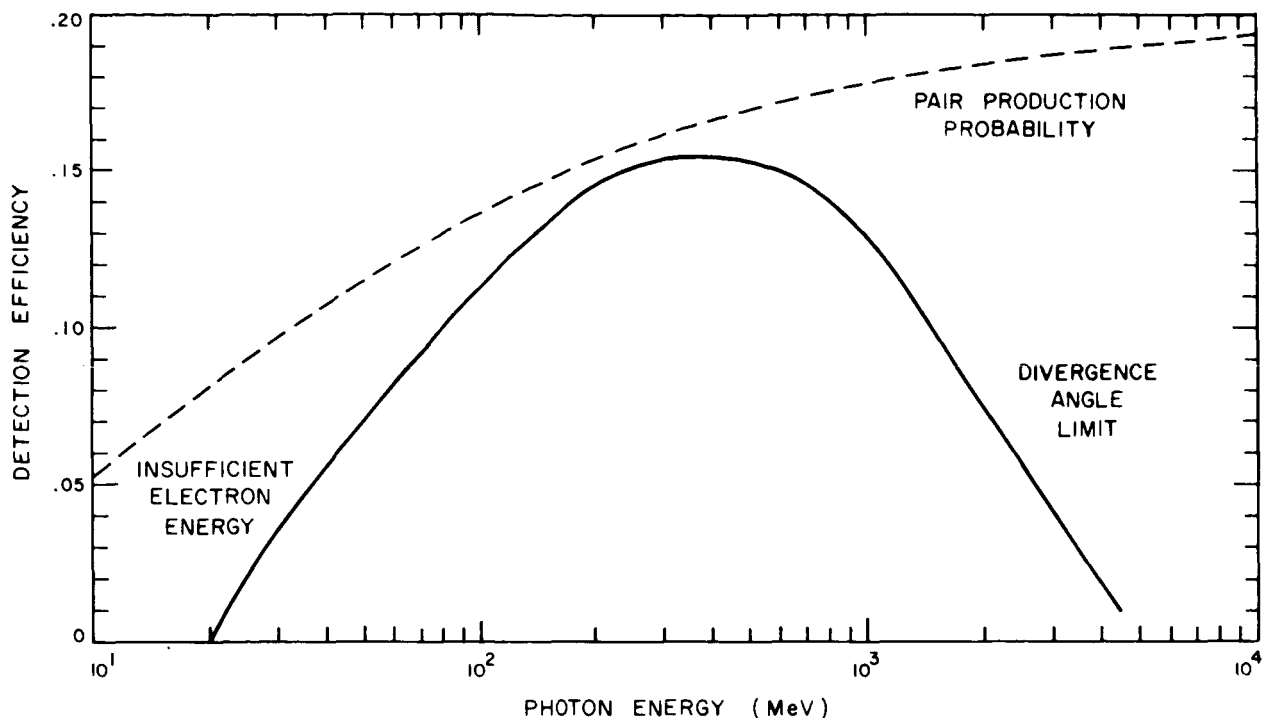
26

Figure 7. Detection efficiency for gamma rays along axis direction of
detector, neglecting edge effects. Criteria for detection
include: a) both electron kinetic energies > 10 MeV, and b)
one gap must contain 2 sparks more than 0.5 cm apart.

The opening angles between the electron and positron tracks have been considered in detail by Olsen (1963). It is clear that after passing through 0.32 cm (1/8 inch) of aluminum, the opening angle is determined primarily by multiple scattering. Neglecting the rare large-angle scattering events, Pinkau (1966a) gives a Gaussian distribution for the projected position of the track-sampling spark in each gap of the spark chamber.

The probability that two sparks are more than a distance S apart (in one projection), $P_1(S)$, for each gap of the chamber, is given by

$$P_1(S) = 1 - (2\pi)^{-1/2} \int_{-\Delta}^{+\Delta} \exp(-\tfrac{1}{2} r^2) \, dr \quad , \tag{2}$$

where

$$\Delta = S(\sigma_1{}^2 + \sigma_2{}^2)^{-1/2} \quad , \tag{3}$$

and σ_1 and σ_2 equal the standard deviation of the projected position of tracks 1 and 2 in the given gap. The probability that they will be separated by more than S in either view is then

$$P_2(S) = P_1(S)[2 - P_1(S)] \quad . \tag{4}$$

Finally, the probability that two separate sparks will be recognized in that gap is

$$P_r(S) = p_s \, P_1(S)[2 - P_1(S)] \quad , \tag{5}$$

where p_s is the probability that sparks form for both tracks in that gap.

The differential cross section for pair production as a function of electron energy fraction was used to obtain an average value of $(\sigma_1{}^2 + \sigma_2{}^2)^{1/2}$, expressed in units of σ_{eq}, the standard deviation of track position for electrons sharing the gamma-ray energy equally. That average was then used in equation (3) to calculate Δ. (See Section 4, Figure 23.)

One clearly resolved double spark is considered necessary and sufficient for recognition of a pair event. The probability Σ_n that an event is recognized in the first n gaps from the plate of origin is found from the recursion relation

$$\Sigma_n = \Sigma_{n-1} + P_r(S_n)(1 - \Sigma_{n-1}) \quad . \tag{6}$$

28

The lower sections of the spark chamber (see Figure 2) have a different structure from the top section, but the scattering in the scintillation counters and thin chamber plates is taken into account by assigning to the lower gaps numbers that give the right track scattering spread, σ. The same σ is assigned to the two gaps in each of the lower pairs of gaps, and the two-spark probability p_s for a single gap is replaced by the probability for two sparks in either gap,

$$p_s(2 - p_s) \quad .$$

The spark formation probabilities were obtained from the scanning sheets containing pair events, on which were recorded the positions of all sparks individually recognized. Care was taken not to bias the sample, in that an opportunity of spark formation was counted only if other sparks clearly showed that there must have been a track present and resolvable. For example, the initial double spark of each event was not included in the sampling, and frequently the last spark of the track was omitted as well. For single tracks the chamber performance was admirable: one spark missing in almost 400 opportunities. With two tracks present however, the probability of two sparks was only 0.56 ± 0.05. Not only would detection efficiency be raised, but the job of scanning the film for pair events would be made vastly easier by increasing this efficiency for two-spark formation. More development work is required in this direction.

There are several ways in which the detection efficiency calculation could be checked or improved.

A. More careful studies could be made of individual events to refine the assumptions made above;

B. Detailed Monte-Carlo programs could be written to generate and "recognize" large numbers of simulated events with a computer, or;

C. The entire instrument could be calibrated in a tagged-photon beam at an accelerator.

Alternative C. is practically equivalent to performing the whole experiment again, and is too costly to justify. Uncertainty over exactly what human scanners will or will not recognize as a good event limits slightly the utility of B., though it should be attempted anyway. If the minimum electron energy is changed, the low energy portion of the efficiency curve should simply move up or down the energy scale accordingly. Changing the effects of scattering on minimum spark separation should move the high-energy end of the curve to higher or lower energies also.

Selected portions of the film were scanned by both scanners independently. Since their event tallies agreed almost perfectly, we are led to believe that their overall scanning efficiency is very high and consistent. Some portions of the film may have had too much noise to be scanned efficiently however. Other effects tend to decrease the efficiency also, such as loss of particles scattered out of the active chamber volume, and at angles away from the axis, attenuation in the glass walls. There is an 80 msec dead time built into the triggering logic, but the actual dead time correction depends on the triggering rate and is not, precisely speaking, part of the detection efficiency. In all, the detection efficiency curve of Figure 7 should be accurate to about 10% from 10^2 to 10^3 MeV, but only about 50% accurate at 50 MeV or 2 GeV.

3.2 Energy Measurements

In gamma-ray detectors, the photon energy may be measured in two basic ways. One is to measure the multiple scattering of each electron to deduce its momentum, hence the momentum of the original photon. The other way is to cause an electromagnetic cascade to form, and measure the total length of electron tracks in the cascade. The kinematic opening angle of the electron pair at production is also a rough measure of photon energy (Olsen, 1963). However, multiple-scattering angles completely dominate over production opening angles for practical balloon-borne detectors. In one sense, observed opening angles produced by scattering provide a measure of that scattering, thus of the photon energy.

Ideally, multiple scattering of the electrons in the many plates of a spark chamber should provide a good measure of the electron momenta. For example, 11 consecutive sparks would give 9 second differences of track position, allowing a momentum measurement accurate to roughly 30%. That assumes that spark measurement errors are negligible. In the present experiment, spark position measurement error is estimated to be at least 1 mm. A serious problem is the absence of some sparks along most pair-electron tracks. One spark missing in the middle of a track eliminates three second differences. Also, missing sparks and overlapping images cause great confusion about the positions and track identifications of sparks near the production vertex. These problems, and the inherent problem of measuring many second differences for each event, persuaded us that the shower counter was a better device for obtaining photon energies.

Hofstadter (1961) has given a general account of the properties of lead-glass Čerenkov counters for measuring photon energies. Such shower counters seldom achieve energy resolutions better than 50% (full width at half maximum). In this experiment, the energy resolution cannot be better than 60%, since the on-axis muons used for gain checks gave a resolution of 50% due to photoelectron statistics. Adding to this the statistical errors in shower development and the shower losses due to electrons entering the counter near its edges, we cannot expect resolution better than 80% (FWHM).

The greatest problem with the shower counter is to obtain an absolute energy calibration. Webber and Chotkowski (1967) calibrated a similar counter, made with 7.2 radiation lengths (10 cm) of SF-6 glass, finding that the pulse corresponding to a muon passing straight through equaled that due to an electron of 240 MeV. In the 10 radiation lengths of the present counter, it is estimated that the muon pulse corresponds to an electron energy of 200 MeV.

An attempt has been made to relate Čerenkov pulse height to electron scattering as revealed by the angle between the two tracks. The result is the scatter plot of Figure 8. Each measurement is subject to at least a factor
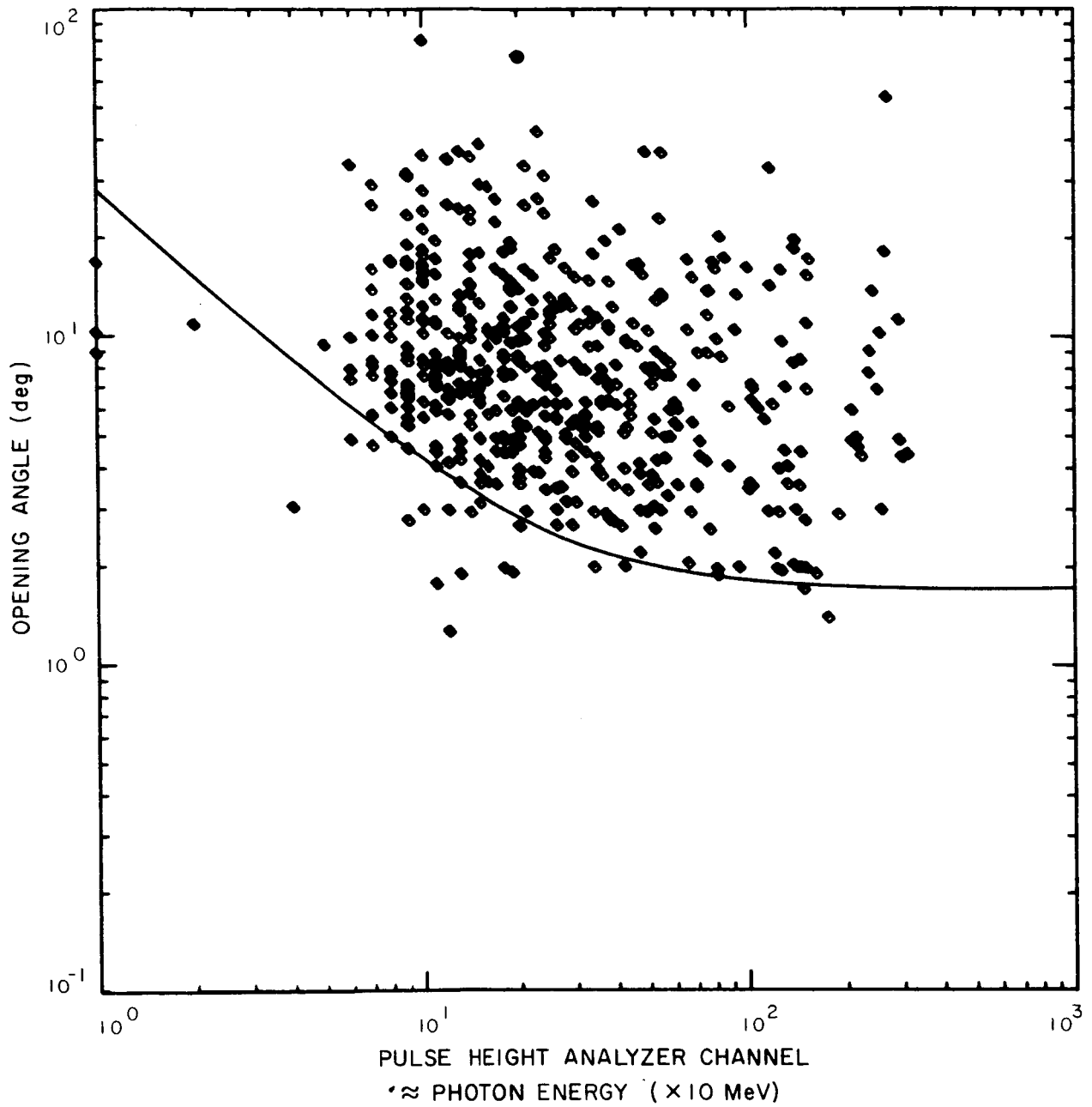
Figure 8. Scatter-plot of opening angle vs. Cerenkov pulse of events observed. Curve is calculated average opening angle vs. photon energy (Section 4, Figure 25).

of two uncertainty. An average relationship between the two measurements was obtained from the integral spectra of pulse-height and reciprocal of opening angle. A relation between pair energy and average opening angle for least-squares fitting of the tracks has also been calculated theoretically (Section 4).

The scatter plot shows a tendency for the measured opening angle to be larger than that calculated, assuming the energy obtained from the pulse height. This is not surprising, considering that the tracks were fitted with a straightedge by visual estimate. Certain events showing an opening angle much greater than expected for the given pulse height were probably nuclear interactions, and not gamma-ray pairs.

An effort is underway to obtain a direct calibration of the Čerenkov counter in a tagged-photon beam. It is hoped that the better calibration and least-squares fitting of the track directions will be able to give a combined measurement of photon energy of 30% accuracy.

3.3 Background Gamma Rays

Primary cosmic rays bombarding the atmosphere of the earth produce high-energy gamma rays, as described in the introduction. These secondary cosmic-ray photons should increase in intensity roughly in proportion to atmospheric depth, for depths on the order of 10 g cm^{-2} or less. As a corollary to this, the intensity should also vary as the secant of the zenith angle.

The present experiment was exposed to the background gamma-ray intensity at $42°$ geomagnetic latitude under $4.0 \pm 0.1 \text{ g cm}^{-2}$ of air for 19,090 seconds. The integral photon spectrum directly measured by the pulse-height analyzer is shown with no corrections in Figure 9. For Figure 10, the muon calibration point has been used to locate the energy scale, and the calculated efficiency vs. energy function has been used to obtain the correct shape of the spectrum. The energy scale was not
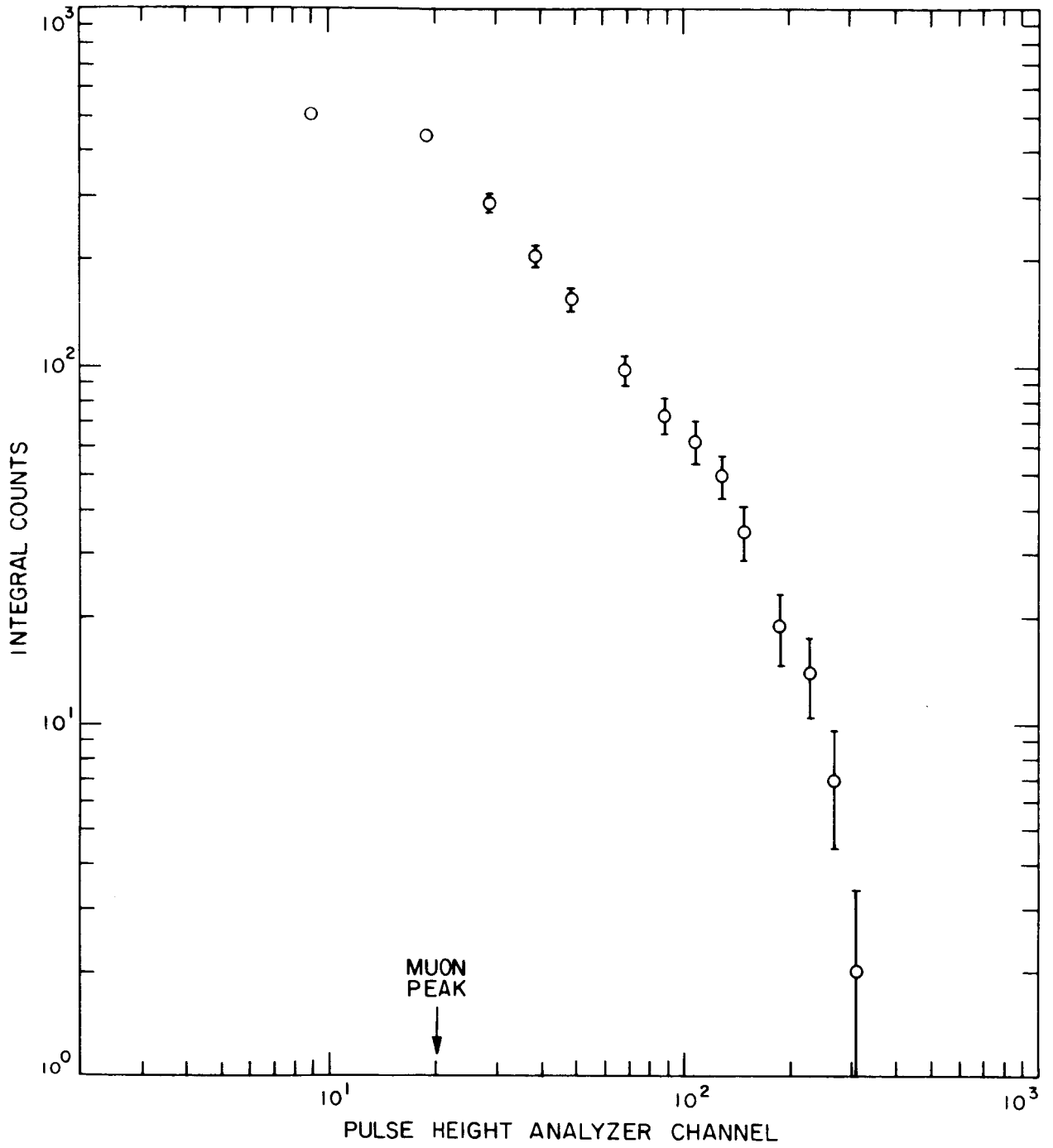
33

Figure 9. Integral pulse-height spectrum. Pulse height of muons used for calibration is indicated.
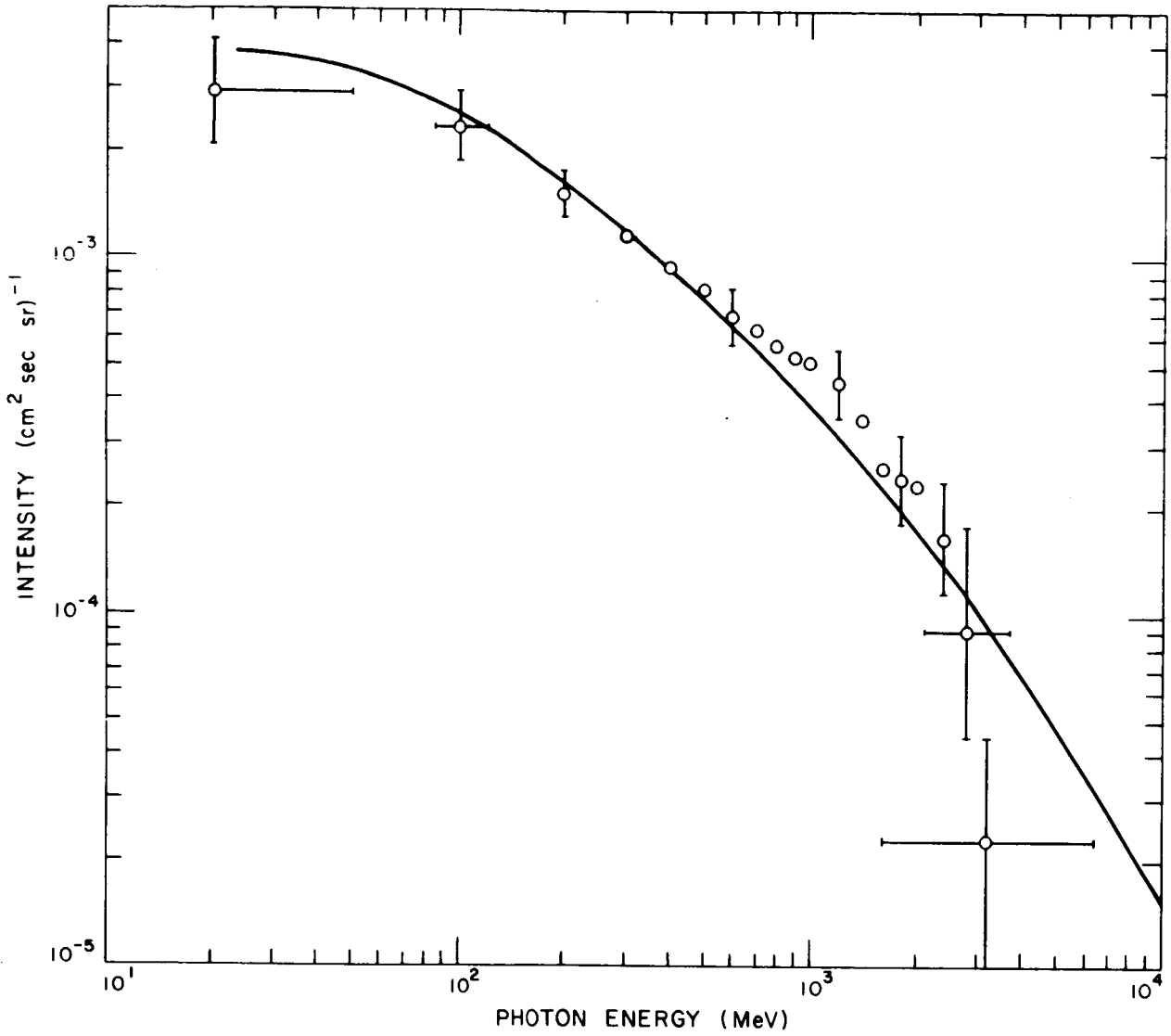
Figure 10. Integral spectrum of pair production events observed
at 4 g cm^{-2} atmospheric depth. Estimated total
errors are indicated for some representative points.
Curve indicates anticipated shape of spectrum.

corrected for loss of shower particles from the $\overset{\scriptscriptstyle\mathsf{Y}}{\mathsf{C}}$ counter, which causes proportionately smaller pulses to be registered for the most energetic photons. The distribution of opening angles is shown in Figure 11.
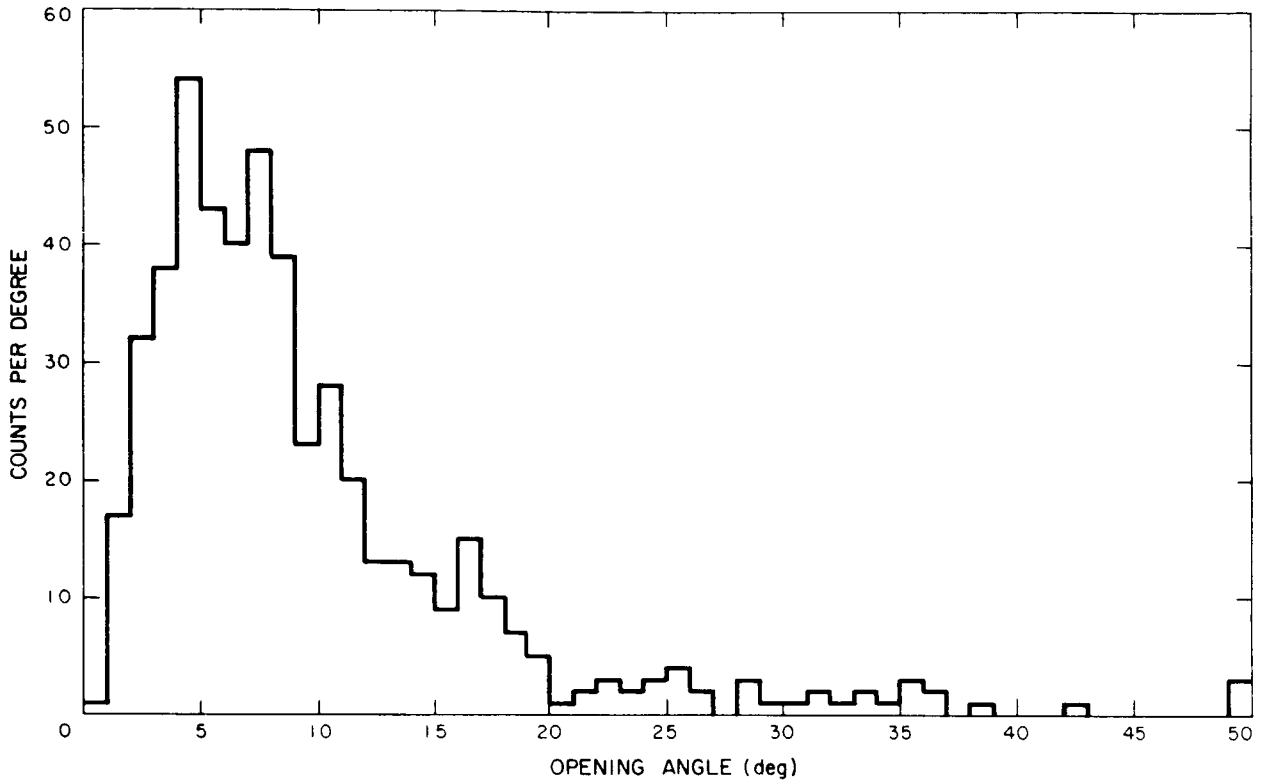
Figure 11. Distribution of opening angles of pair-production events.

Figure 12 gives the distribution of pair bisectors in zenith angle bins of equal solid angle. The counts fit the calculated effective area vs. zenith angle curve reasonably well. However, for zenith angles greater than $\sim 25°$, the efficiency falls off due to edge effects and attenuation in the chamber walls. Beyond 40°, where the calculated effective area is very small, a few excess counts are contributed by scattering from smaller zenith angles. The statistics are not good enough either to derive a better effective area curve, or to check for a secant dependence of the intensity.
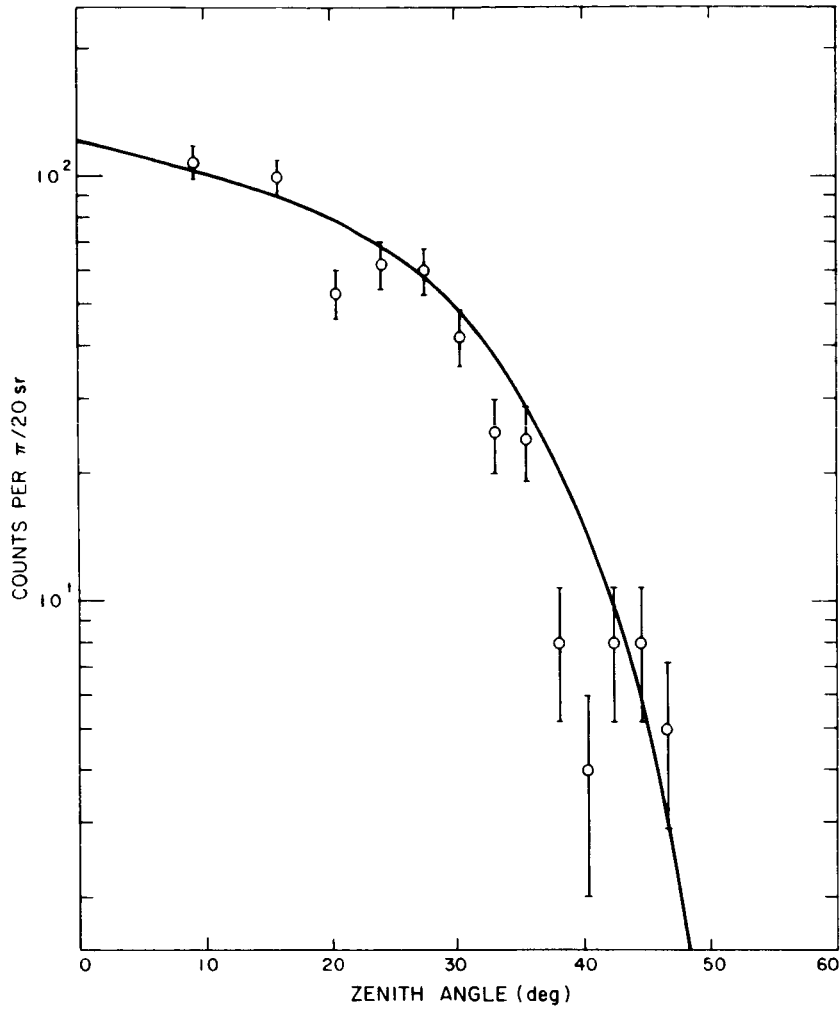
Figure 12. Zenith angle distribution of pair-production events.
The curve is the calculated effective area of the
detector, adjusted in height.

The effective area curve (Figure 5) was used to calculate the observed
intensity as a function of zenith angle. The detection efficiency used was
0.12, corresponding to 110 MeV photon energy. Weighting most heavily
the points obtained at less than 30° zenith angle, we find for the overhead
gamma-ray intensity

$$(2.7 \pm 0.2) \times 10^{-3} \ (cm^2 \ sec \ sr)^{-1} \quad .$$

For all zenith angles observed, the ratio of counts from the west to counts from the east was 0.95 ± 0.13.

3.4 Upper Limits on Fluxes

In order to search for discrete celestial sources of gamma rays, the cone of angular resolution of the detector must be made small to reduce the background counts that will mask possible source counts. That is, the signal-to-noise ratio is better for smaller resolution cones. The improvement is slight however, once the background intensity contributes only a few counts per resolution cone per exposure.

The problem of the angular resolution of the present detector is considered carefully in Section 4. The ability to resolve both tracks of an electron pair gives us a convenient way of defining a resolution cone for each individual event. The most probable direction of the incident photon is the bisector of the two electron track directions. The resolution cone is defined so that 50% of the photons from a given source direction will produce bisectors within the resolution cone angle of that direction. The intrinsic resolution cone angle is about 1/2 the average opening angle of the pair. To this must be added the errors in navigation, i.e., spark chamber position determination.

When searching for gamma rays from some celestial object, a photon is counted as coming from that source if its track bisector is within its resolution angle of the source direction. The photons are counted as a function of maximum allowed resolution cone. For each resolution cone r, the expected background counts are found by counting the events of cone angle between r and r + Δr in the surrounding sample of sky, and multiplying by the ratio of resolution cone solid angle to the solid angle of sky sampled. The background numbers are then added up to find the total expected background as a function of maximum resolution cone. The two sets of numbers, source counts and expected background counts, are compared in Figure 13 for the Crab Nebula, and in Figure 14 for the sun (whole exposure).

Following the integrated-likelihood method suggested by Kenneth Greisen (private communication), we may deduce the maximum number of photon counts that should be received from the chosen source in any given percentage of identical repeated experiments. This is called the upper limit of the source counts with that percentage of confidence. Let N be the number of counts observed from the source direction. The expected number of background counts is B, and S is the hypothetical expected number of source counts, on the average. Then the a priori probability of N counts is

$$p(N) = \frac{(S + B)^N}{N!} \, e^{-(S+B)} \quad . \tag{7}$$

The probability $P(N, S_0, B)$, that for the given N and B the average source number S is greater than S_0 is

$$P(N, S_0, B) = e^{-S_0} \sum_{i=0}^{N} \frac{(S_0 + B)^i}{i!} \bigg/ \sum_{j=0}^{N} \frac{B^j}{j!} \quad . \tag{8}$$

Upon setting $S_0 = 0$, it is seen that $P(N, S_0, B)$ is correctly normalized. A value is now chosen for $P(N, S_0, B)$, say 0.05 for a 95% confidence limit, and equation (8) is solved for S_0. This process has been carried out for P = 0.05 and representative values of B and N; Figure 15 displays the resulting values of S_0.

To obtain the upper limit of the source flux, the pure number S_0 is divided by the exposure and efficiency:

$$F_{lim} = \frac{2 S_0}{\epsilon \, A \, T \, t} \quad . \tag{9}$$

The factor 2 is used here because the resolution cone in this experiment is defined to contain only half of the source photon events. The average detection efficiency for the energy range considered is ϵ, the integrated area-time exposure product for that source is A T, after subtraction of dead-time, and t is the transmission of the overlying atmosphere.

In contrast to the usual method, of subtracting background after finding an upper limit for the total number of events from the source direction from an integrated Poisson distribution, the integrated-likelihood method never gives a negative result for S_0. It may be observed from equation (8) that for N = 0, S_0 is independent of B (S_0 = 3.0 for 95% confidence), and it never reaches smaller values. Also, for each N, S_0 tends toward this value as B increases. We conclude that no experiment could report a 95% confidence upper limit smaller than

$$F_{min.\ lim}\ (0.95) = \frac{3.0}{\epsilon' A T t} \quad , \quad (10)$$

where ϵ' is the detection efficiency, including the probability for a source photon to be contained in the resolution cone of the detector.

A map of photon events from near the Crab Nebula is shown as Figure 16. It is seen from Figure 13 that the great majority of photon events have resolution cones less than 10°. For a maximum resolution cone of 10°, we have an upper limit of source counts from the Crab Nebula of 4.9 photons. This number does not depend strongly on what limit is chosen for the resolution cone. The exposure of the Crab Nebula, A T, equaled 1.06×10^6 cm^2 sec after dead-time correction. The majority of photons detected had energies less than 200 MeV. Accordingly, we take the average detection efficiency to be 0.12, its value at 110 MeV. Then from equation (9), we find the 95% confidence upper limit of integral flux from the Crab Nebula to be:

$$F_{lim}(Crab) = 8.7 \times 10^{-5} \ (cm^2 \ sec)^{-1} \quad .$$

The corresponding threshold energy is 100 MeV.

Photon events from near the sun are mapped in Figure 17. The same procedure followed for the Crab Nebula was used to find the upper limit of average gamma-ray flux from the sun. We find 6.5 to be the upper limit number of photons received from the sun during the whole flight. The exposure, A T, in this case is 1.30×10^6 cm^2 sec. Again taking ϵ = 0.12, the upper limit of photon flux above 100 MeV energy from the sun is

$$F_{lim}(sun) = 9.4 \times 10^{-5} (cm^2 \ sec)^{-1} \quad .$$

Solar flares did occur while the detector was at float altitude (ITSA, 1966). Therefore, the chronology of the observed solar flares, of importance S, 1, and 2, was compared with that of the gamma rays from the solar direction (see Figure 18). The gamma rays appear to come just after the peak optical intensity of the flares, during the radio burst. All of the counts occurred during flares, but this was quite likely to happen at random, due to atmospheric background.

Two of the gamma rays, however, arrived just before or at the start of Type III radio bursts from the importance 1 and 2 flares. Since the bursts are of such short duration, the a priori probability of background events coming so close to the time of the flare burst is quite small. For the first photon, of 660 MeV energy, the random probability is 2×10^{-3}. For the second, of 110 MeV, the probability is 3×10^{-2}. While there were not enough counts to draw any definite conclusions, a strong suspicion is aroused that Type III radio bursts are often accompanied by "flashes" of gamma rays of greater than 100 MeV energy. To test this hypothesis, a gamma-ray detector of good angular resolution and very large area must be flown during solar flares.

Preliminary data from the OSO-III gamma-ray experiment (George Clark, private communication) suggested the possibility that this balloon experiment may have been able to detect a gamma-ray flux from the Galaxy as a whole. The photon events from the flight were transformed to galactic coordinates and sorted into bins of equal solid angle. An exposure and an intensity were calculated for each bin, and for bands of equal galactic latitude (Figure 19).

For the equatorial plane, $-13.8° < b^{II} < +13.8°$, near the anticenter of the Galaxy, $75° < \ell^{II} < 215°$, we observe a total gamma-ray intensity (> 100 MeV) of $(2.0 \pm 0.2) \times 10^{-3} (cm^2 \ sec \ sr)^{-1}$. For all other directions, the intensity averages $(2.1 \pm 0.1) \times 10^{-3} (cm^2 \ sec \ sr)^{-1}$. Thus no galactic

flux is observed. The 95% confidence upper limit, corresponding to 1.64 standard deviations, of gamma-ray intensity from the indicated galactic directions is 2.7×10^{-4} $(cm^2 \ sec \ sr)^{-1}$.

Reasonable limits can be put on gamma intensities from moderately extended sources because the counting statistics are better than for point sources. In this case, 173 counts were observed near the galactic plane, while 181 were expected as background from the earth's atmosphere.

(Note: the intensity calculations for Figure 19 did not include deadtime corrections. The numbers quoted above do include all known correction factors.)
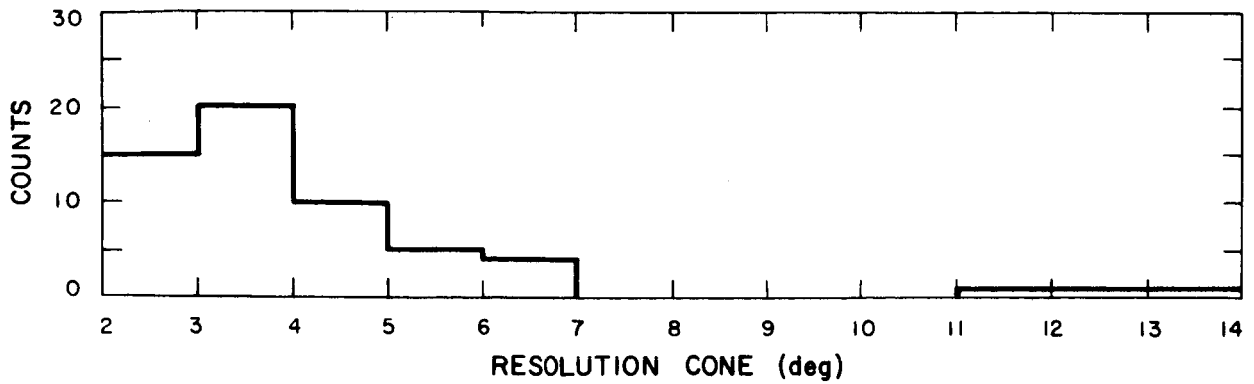
Figure 13a. Events within 20° RA and 20° declination of Crab Nebula vs. resolution cone angle.
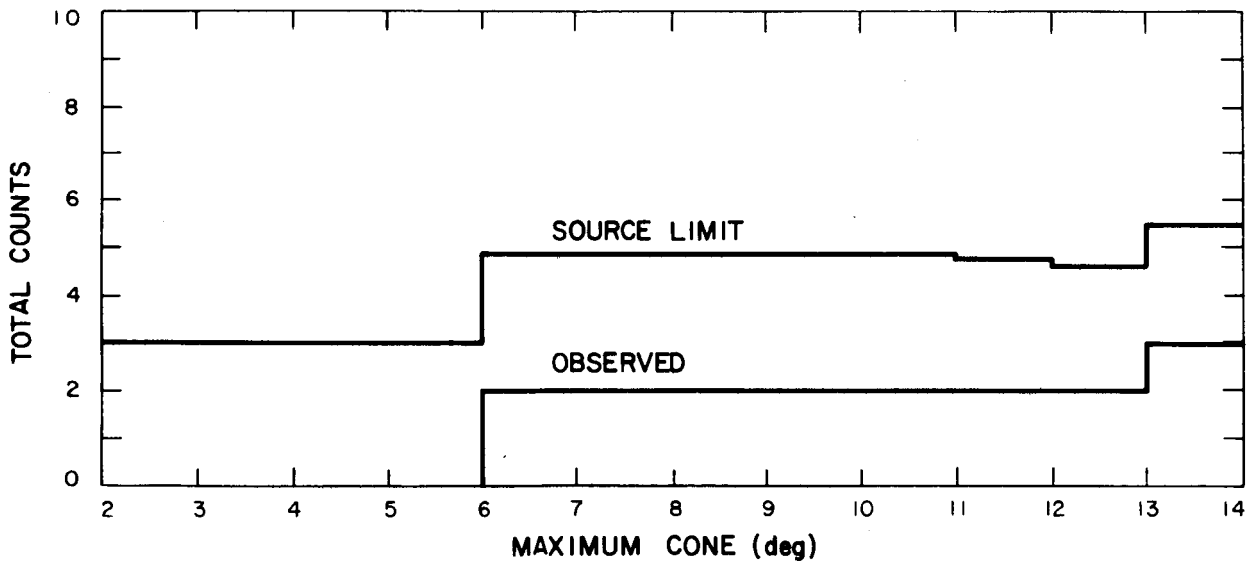
Figure 13b. Integral numbers of events observed and upper limit of source counts (95% confidence) vs. maximum resolution cone angle.
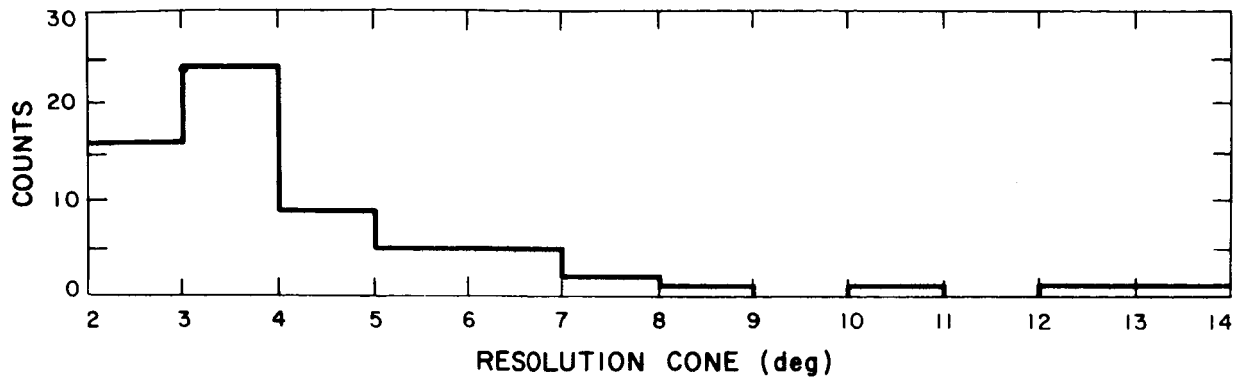
43

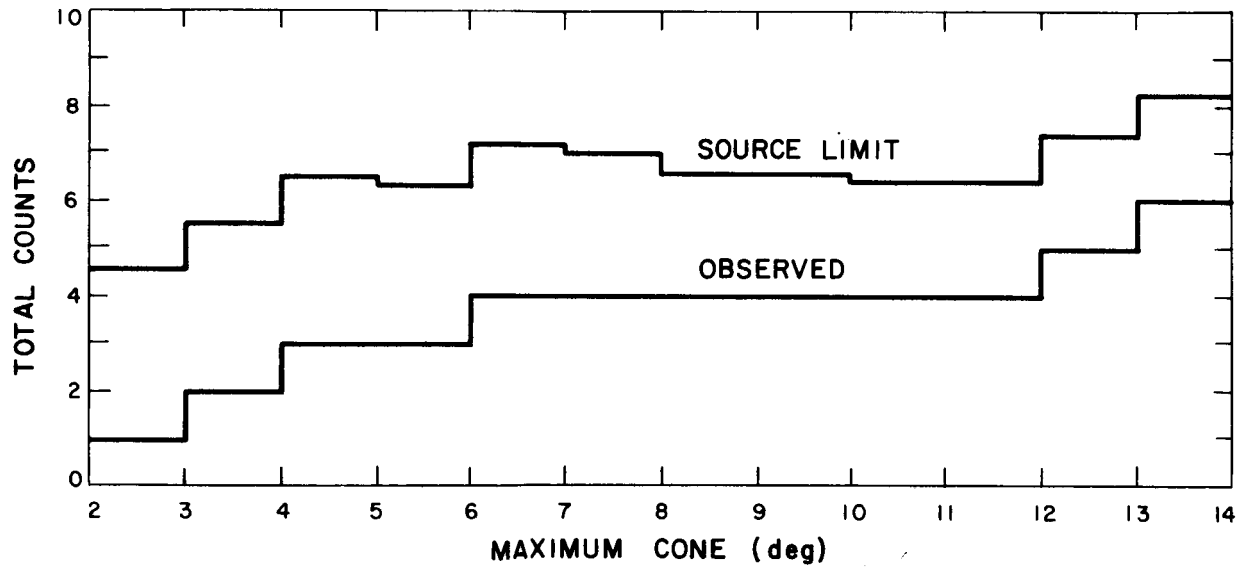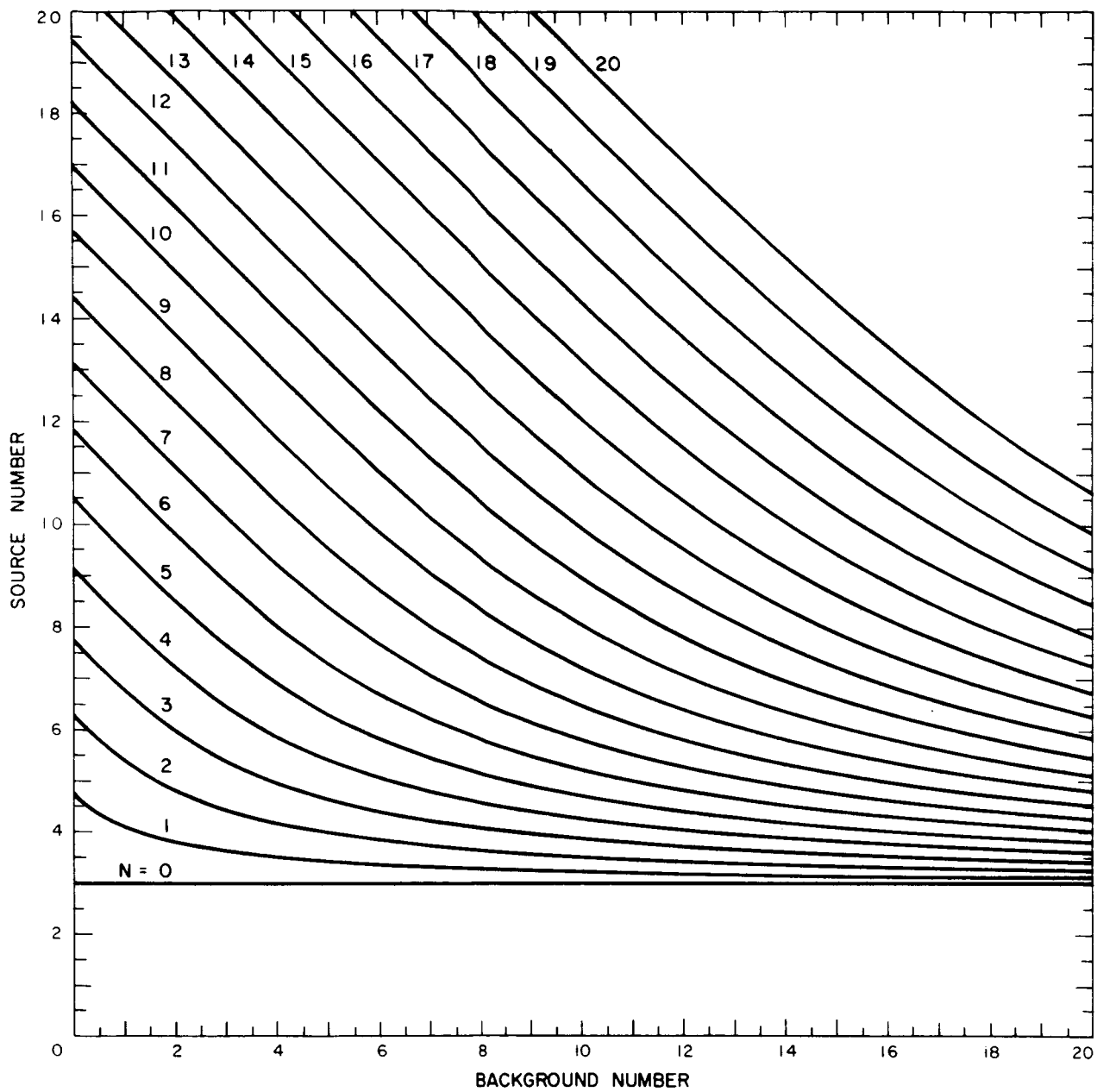Figure 14a. Events within 20° RA and 20° declination of sun vs. resolution cone angle.

Figure 14b. Integral numbers of events observed and upper limit of source counts (95% confidence) vs. maximum resolution cone angle.

Figure 15. Upper limit of source counts (95% confidence) vs. background,
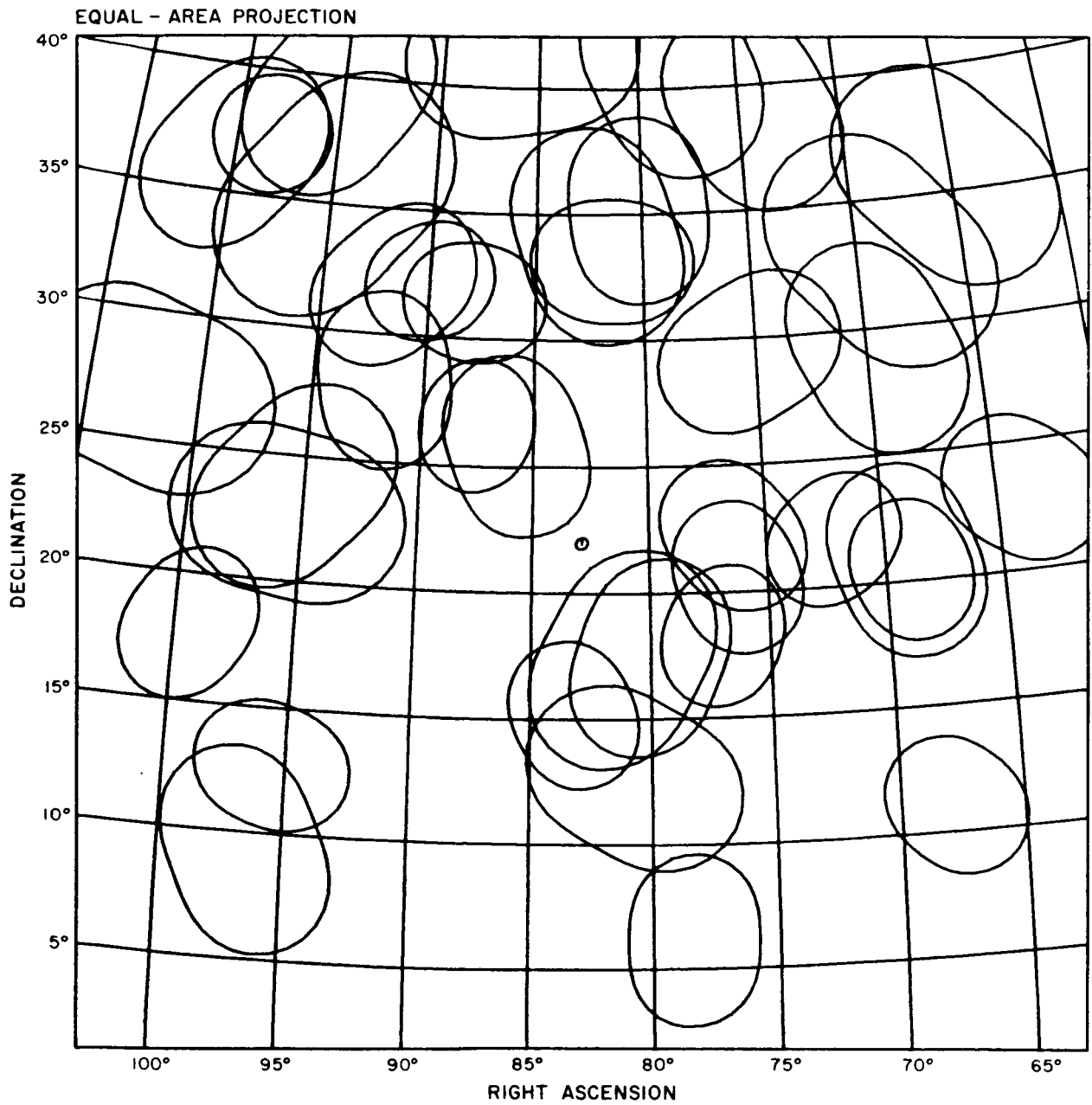for N observed counts.

Figure 16. Celestial map of gamma ray events near the Crab Nebula. The probability that any photon arrived from within its indicated resolution contour is 1/2. Only events of opening angle < 10° are shown.
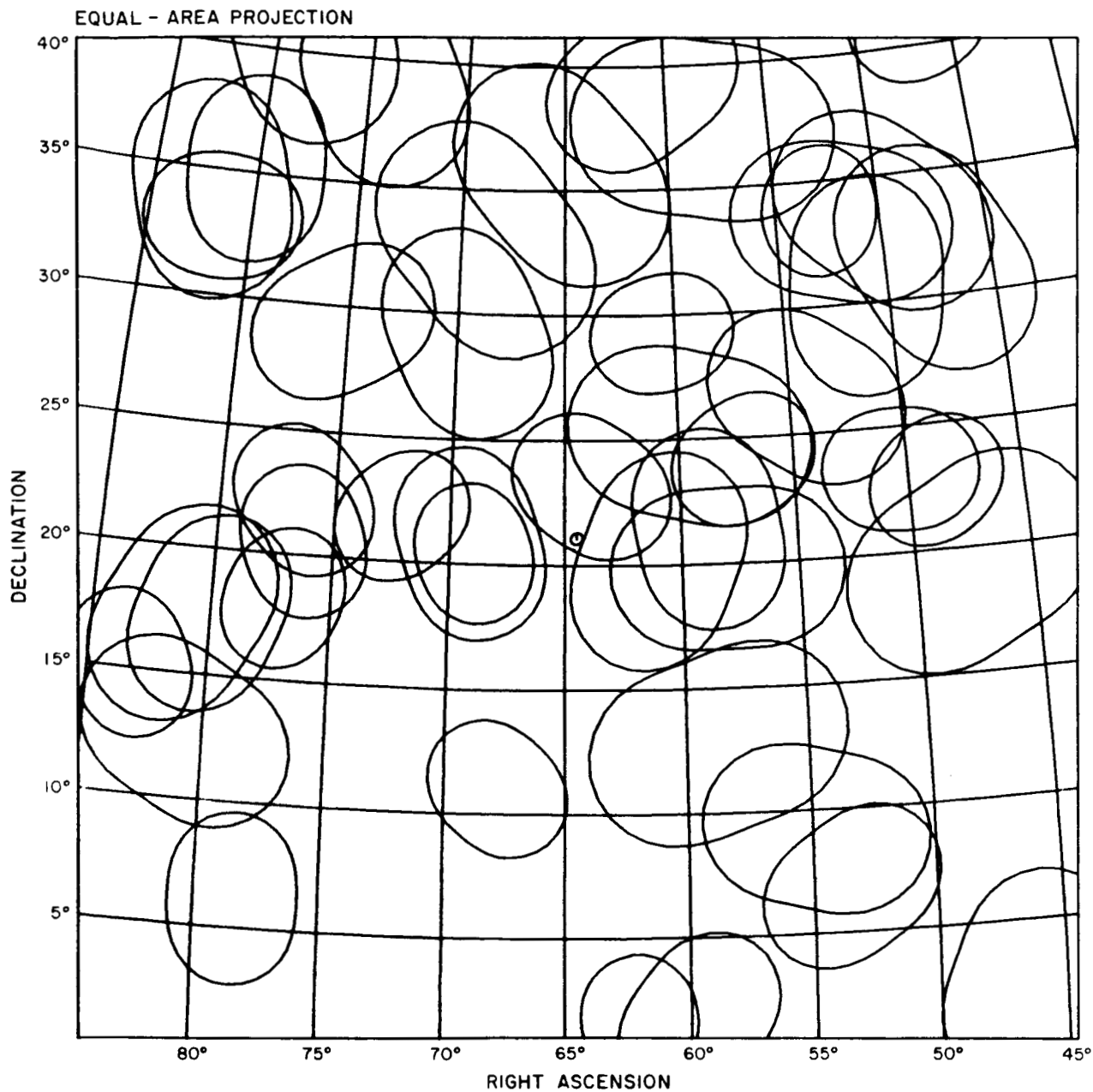
46

Figure 17. Celestial map of gamma ray events near the sun. The probab-
ability that any photon arrived from within its indicated
resolution contour is 1/2. Only events of opening angle < 10° are
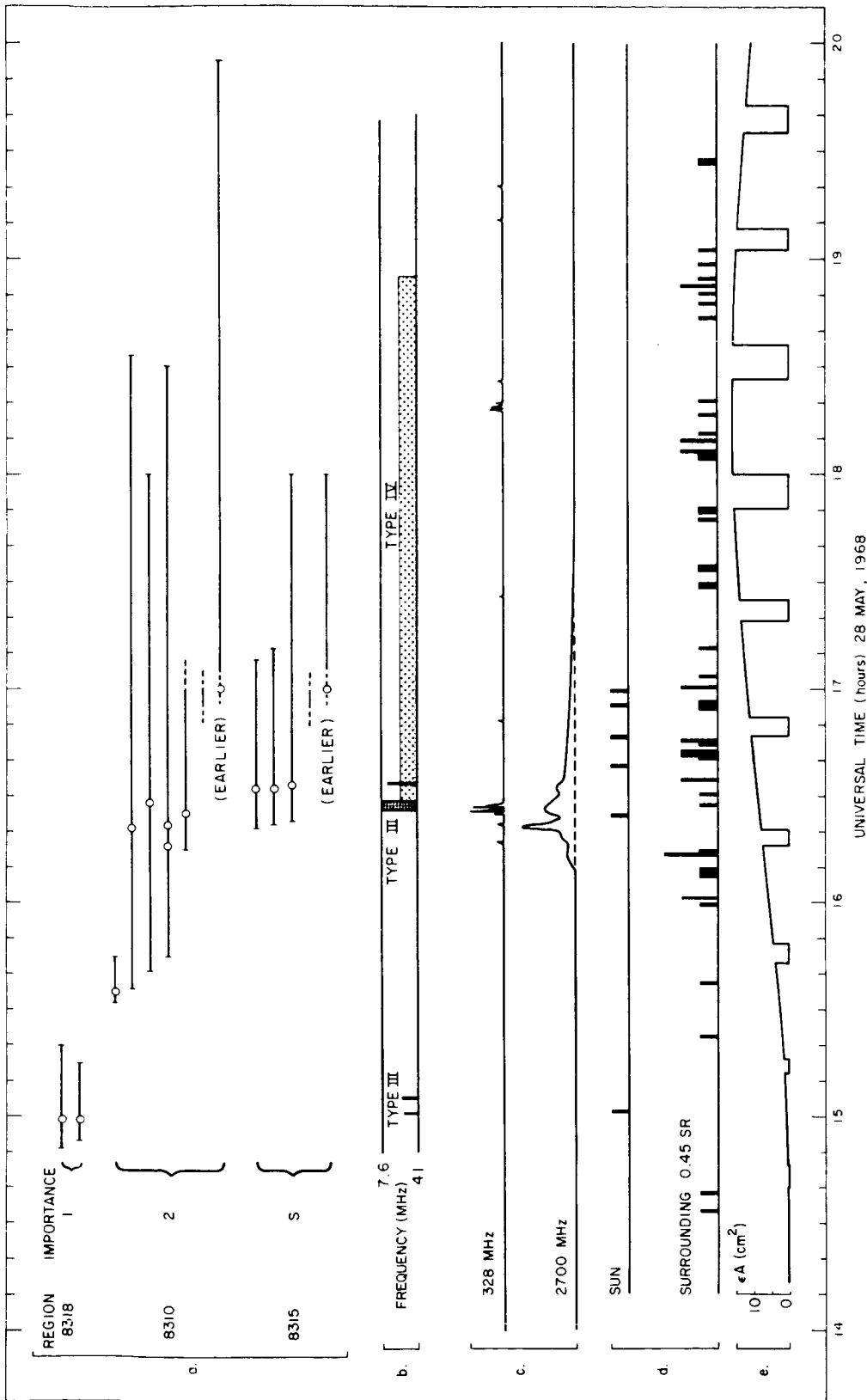shown.

47

Figure 18. Chronology of solar events.

    a. Optical observations of flares in given McMath plage region, showing time of maximum brightness (circles) (ITSA, 1966).

    b. Radio bursts observed by University of Colorado between 7.6 and 41 MHz (ITSA, 1966).

    c. Radio emission observed at 328 and 2700 MHz (PENN, 1966).

    d. Gamma ray counts from sun direction and surrounding area.

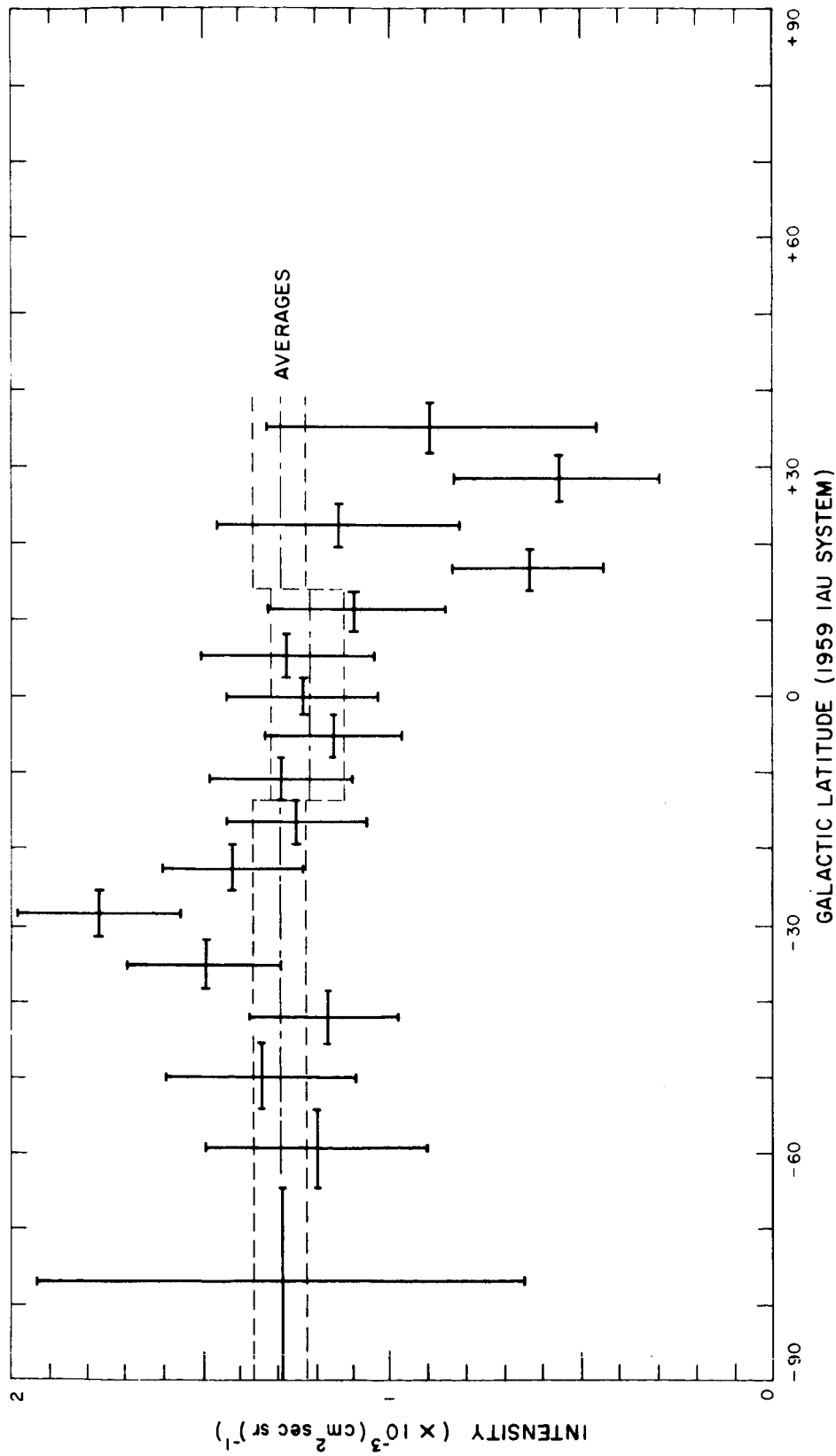   e. Efficiency times area of gamma-ray detector presented to sun.

48

Figure 19. Gamma ray intensity vs. galactic latitude. Longitudes observed range from 75° to 215°. Errors shown are due to counting statistics only.

4. ANGULAR RESOLUTION OF THE DETECTOR

In principle, it should be possible to find very accurately the energy and direction of an incident photon by reconstructing its momentum from the momenta of the pair-produced electron and positron, since the momentum of the recoiling nucleus is quite small relative to the electron momenta, at the energies considered here. However, no matter what material is used for converting the photon by pair production, the electrons (+ and -) suffer multiple Coulomb scattering in the converter, which limits the accuracy of measurements of their directions. This is unavoidable because both multiple scattering and pair production probability depend on the thickness of the converter, L, as measured in radiation lengths.

Since the mean squared scattering angle is proportional to L, so is the solid angle contributed by scattering to the resolution cone. This means that for L considerably less than one radiation length, the number of gamma rays detected from a point source is proportional to L, while the number of photons of a diffuse background intensity detected within the resolution cone is proportional to L^2. For the best signal-to-noise ratio, L must be made small. On the other hand, as the discussion of upper limit flux determinations in Section 3.4 makes clear, the statistical improvement is slight once there are only a few events per resolution cone.

While the detection efficiency per unit area, ϵ, is proportional to L for small L, the product ϵA entering into all flux expressions may be maintained by distributing the same amount of converter material over a larger area as L is decreased. A somewhat different approach is to incorporate the converter in the direction-determining device. Though the same amount of converter may be present, the track directions are revealed where the electrons have traversed only a small amount of converter. This is called an extended converter. The ultimate in extended converters is represented by the

photographic emulsion. In it, the electron track directions can be measured before they are badly scattered, regardless of total converter thickness. Also, multiple scattering within the converter gives a measure of each electron's momentum. The narrow-gap spark chamber retains these advantages of the extended converter, while allowing rejection of background events by counters and logic circuitry.

The problem of determining the starting position and direction of a particle track observed in a narrow-gap spark chamber has been considered in detail by Pinkau (1966a and b, 1968). The formulae obtained by Pinkau take into account multiple scattering, as formulated by Molière, and random errors in spark position measurements. The initial sparks of the track are weighted more heavily in the least-squares fit. It is assumed that the tracks are nearly perpendicular to the plates.

The formula of interest here is for the angle of a track in one projection, where the positions of the k sparks z_n, n = 1 to k, have been measured along the gaps in that projection. The maximum likelihood initial angle of the track is

$$\phi_m = \frac{Z_1 N_0 - Z_0 N_1}{\Delta(N_2 N_0 - N_1^2)} \quad , \tag{11}$$

where

$$N_0 = \sum_{n=1}^{k} D_n \quad , \tag{12a}$$

$$N_1 = \sum n D_n \quad , \tag{12b}$$

$$N_2 = \sum n^2 D_n \quad , \tag{12c}$$

$$Z_0 = \sum z_n D_n \quad , \tag{12d}$$

$$Z_1 = \sum n z_n D_n \quad , \tag{12e}$$

$$D_n = (\zeta_d^2 w_n + 2 \sigma_z^2)^{-1} \quad , \tag{13}$$

and

$$w_n = \frac{1}{4} nd(\Delta^2 + \frac{1}{3} d^2) + \frac{1}{3}(n + 1)n(n - 1) d\Delta^2 \quad . \tag{14}$$

The standard deviation of spark position measurements is σ_z, the center-to-center gap spacing is Δ, and d is the plate thickness (all in centimeters). The multiple scattering effects are contained in the quantity ζ_d, which is given in CGS units by:

$$\zeta_d^2 = \frac{112}{X_0 \ln(183 Z^{-1/3})} \frac{z^2}{(pv)^2} B_d \quad . \tag{15}$$

In equation (15), Z is the atomic number of the plate material, X_0 is the radiation length in centimeters, z is the charge of the particle, and pv its momentum times its speed, in MeV. The quantity B_d is obtained from:

$$\frac{1}{B_d} e^{B_d} = 6.68 \times 10^3 \frac{dpC}{\beta^2} \quad , \tag{16}$$

$$C = \frac{(Z + 1) Z^{1/3} z^2}{A(1 + 3.34 a^2)} \quad , \tag{17}$$

$$\alpha = \frac{zZ}{137} \quad , \tag{18}$$

and

$$\beta = \frac{v}{c} \quad .$$

In equations (16) and (17), ρ is the density in g cm^{-3} and A the atomic weight of the plates.

For the spark chamber of this experiment, with 1/8-inch-thick aluminum plates, 1/4-inch gaps, and scattering fast electrons ($z = 1, \beta = 1$), we find the following values:

$$\Delta = 0.95 \text{ cm}$$
$$w_n = .097 \, n^3 - .022 \, n \approx .097 \, n^3 \quad ,$$
$$B_d = 11.23 \quad ,$$

and

$$\zeta_d^2 = 32.6 \, (pv)^{-2} \quad ,$$

where (pv) is in MeV. From inspection of spark images on the kinerecorder film, σ_z was estimated to be 0.1 cm.

If formula (11) is used for ϕ_m in the analysis of data, missing sparks can be taken into account by omitting from the sums of equations (12a to e) the terms of those n corresponding to the missing sparks.

An equally important quantity may be obtained from the Pinkau results. It is the "standard deviation," or more correctly, the deviation from ϕ_m which has a likelihood $e^{-1/2}$ that of ϕ_m. It is

$$\sigma_\phi = (\Delta \sqrt{2\, N_2})^{-1} \quad \text{(radians)} \quad .$$ (19)

The quantity σ_ϕ, in degrees, is plotted as a function of electron kinetic energy for various numbers of gaps, k, in Figure 20.

The portion of the spark chamber below counter B1 in this experiment has a different structure from the upper chamber, but together with the scintillators, it produces roughly the same scattering effects as if it were a continuation of the upper chamber. Therefore, in calculating the track angle errors, the formulae for the upper section were used throughout. For example, k was assumed to be equal to 6 or 8 for all events, even those originating in the last thick plate before B1.

The least-squares track fitting procedure in the foregoing gives the lower limit of error for any method. In the present experiment, the tracks were fitted simply with a line drawn "by eye" by a physicist. This subjective procedure sometimes approaches a least-squares fit, while consuming much less time than individual spark measurements would require. However, if a technique is used which automatically provides spark positions in digital form, the least-squares analysis by computer is simple and rapid.

Having determined the initial directions of the electron tracks, with a standard deviation for each, the next procedure is to reconstruct the total momentum vector, $\vec{P}_e$, of the two electrons. Since the scattering errors in $\vec{P}_e$ are much greater than the nuclear recoil momentum, $\vec{P}_e$ may be equated with $\vec{k}$, the gamma-ray momentum. Figure 21 diagrams the situation, with the angles exaggerated for clarity. For small opening angles, θ, we have

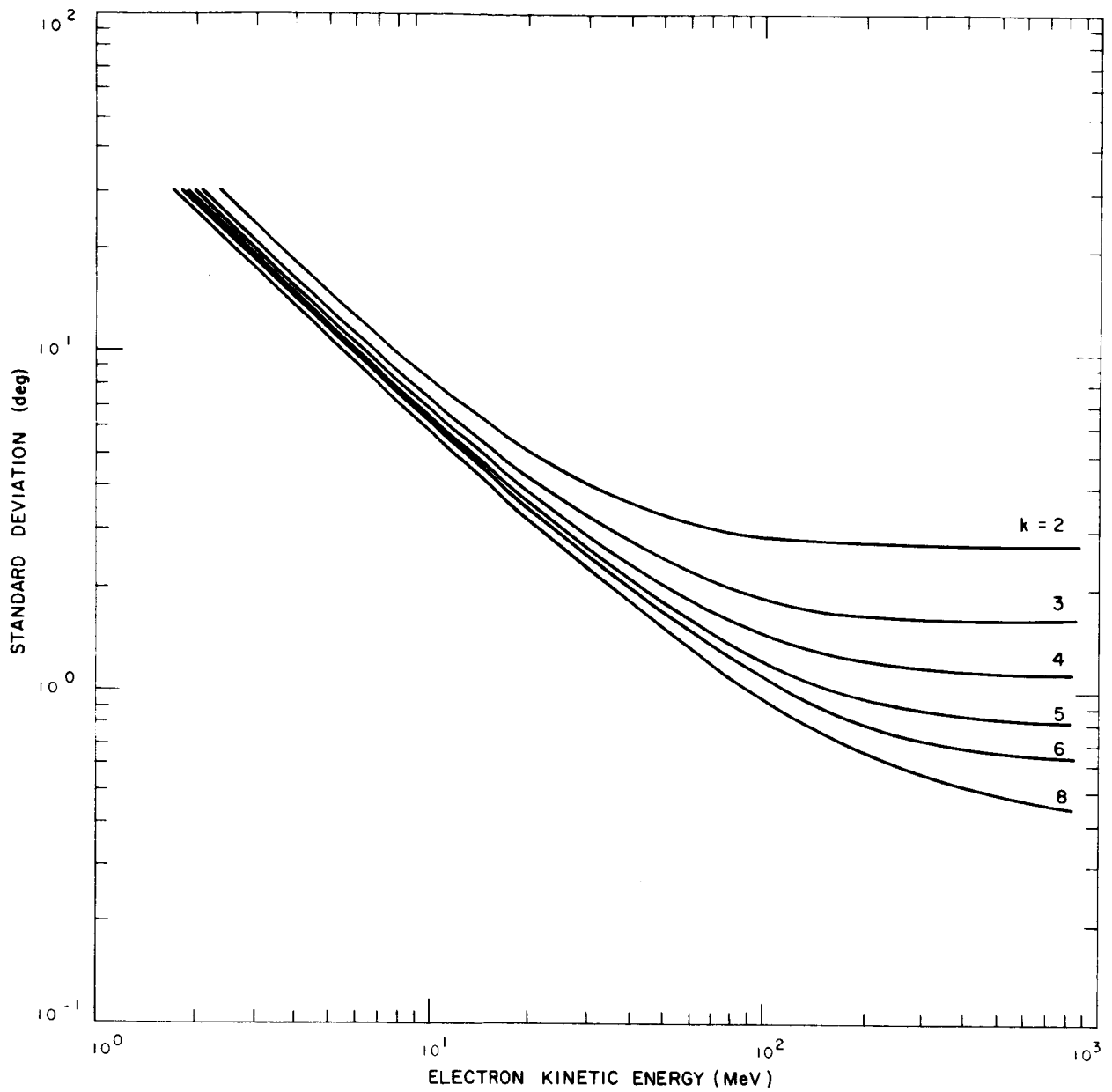$$\frac{\alpha_i}{\theta} \approx 1 - \frac{p_i}{k} \quad .$$ (20)

Figure 20. Standard deviation of electron track angle determination vs. electron energy. Number of sparks measured is k.

From the differential cross section for pair production (Rossi, 1952), it is seen that all values of p_i/k have approximately the same probability, so for a given θ, all values of a_i/θ have approximately the same probability.
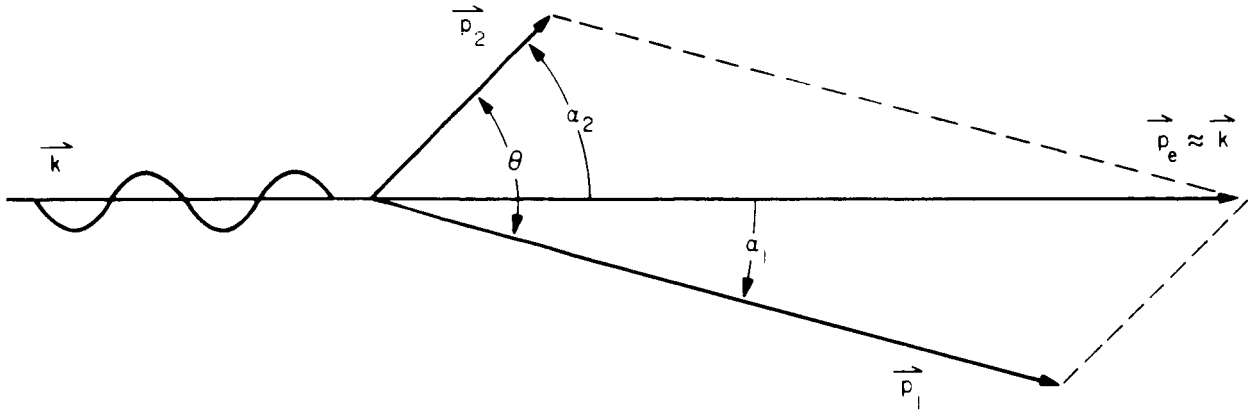

Figure 21. Reconstruction of photon momentum.

Assuming values for k, p_1, and p_2, we wish to find the error in the direction of $\vec{k}$. This is obtained from

$$(\Delta\vec{k})_{\perp} = p_1 \, \Delta\vec{a}_1 + p_2 \, \Delta\vec{a}_2 \quad ,$$ (21)

where the $\Delta\vec{a}_i$ are the angular errors of the electron tracks. Since they are caused by multiple scattering for most events in this experiment, we have

$$\Delta a_i \propto \frac{1}{p_i} \quad .$$ (22)

Thus on the average, $(\Delta k)_\perp$ is independent of (p_1/k). Then we need to consider only the equipartition case, $p_1 = p_2 = k/2$. We have

$$\left\langle \left(\frac{\Delta k_\perp}{k}\right)^2 \right\rangle = \frac{\langle (\Delta a)^2 \rangle}{2} \quad , \tag{23}$$

or

$$\delta_\gamma = \frac{(\Delta a)_{rms}}{\sqrt{2}} \quad , \tag{24}$$

where δ_γ and $(\Delta a)_{rms}$ are the root-mean-square errors in the direction measurement of the photon and an electron of momentum $p = k/2$, respectively.

What is desired is the probability distribution of the incident photon direction, without assuming knowledge of the electron momenta. In this experiment, only θ is known directly, though k can be inferred from the pulse height in the shower counter. For a given value of p_1/k, hence given a_1/θ, the photon direction distribution is

$$P_a(x, y) = \frac{1}{2\pi \sigma^2} e^{-[(x-a)^2 + y^2]/2\sigma^2} \quad , \tag{25}$$

where

$$\sigma = \frac{\sigma_{eq}}{\sqrt{2}} \quad . \tag{26}$$

In equation (26), σ_{eq} is the standard deviation of the projected angle of either electron track, in the case of equipartition of the photon energy. The angle variables x, y, and a are explained by Figure 22.
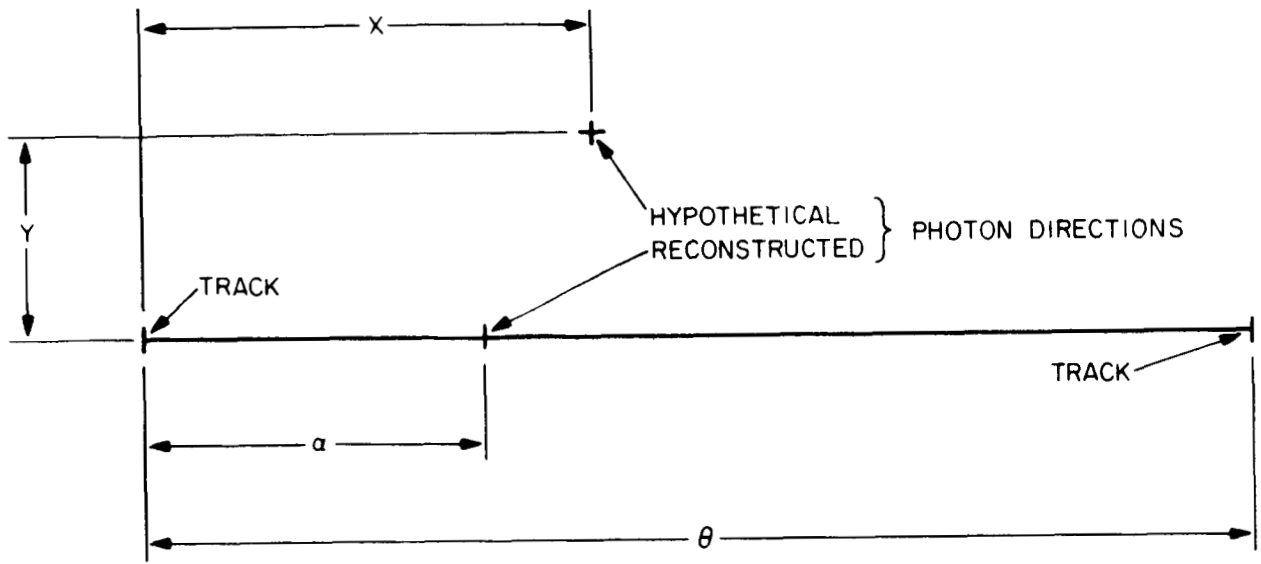
Figure 22. Definitions of angles used in resolution calculations.

Since the value of a/θ is not known, an integration over a is required:

$$P(x, y) = \frac{1}{2\pi \sigma^2} e^{-y^2/2\sigma^2} \int_0^{\theta} P(a) e^{-(x-a)^2/2\sigma^2} \, da \quad . \tag{27}$$

Since

$$P(a) \approx \frac{P\left(1 - \frac{P_1}{k}\right)}{\theta} \approx \frac{1}{\theta} \quad , \tag{28}$$

we obtain the approximation

$$P(x, y) \approx f\left(\frac{x}{\sigma}\right) g\left(\frac{y}{\sigma}\right) \quad , \tag{29}$$

where

$$g(\frac{y}{\sigma}) = \frac{1}{\sigma\sqrt{2\pi}} \, e^{-y^2/2\sigma^2} \quad , \tag{30}$$

and

$$f(\frac{x}{\sigma}) = \frac{1}{\theta\sqrt{2\pi}} \int_{(x-\theta)/\sigma}^{x/\sigma} e^{-t^2/2} \, dt \quad , \tag{31a}$$

or

$$f(\frac{x}{\sigma}) = \frac{1}{2\theta} \left[\frac{1}{\sqrt{2\pi}} \int_{-x/\sigma}^{+x/\sigma} e^{-t^2/2} \, dt - \frac{1}{\sqrt{2\pi}} \int_{-(x-\theta)/\sigma}^{+(x-\theta)/\sigma} e^{-t^2/2} \, dt \right] . \tag{31b}$$

The integrals in equation (31b) are found in tables (Dwight, 1961).

The most likely direction for the incident photon is the bisector of the electron track directions (x = θ/2, y = 0). It is found for $\theta < \sim 3\sigma$ that within a very small error ($\sim$ 1%) the f(x/σ) distribution is Gaussian. Changing to x' = x - θ/2, we may express P as

$$P(x', y) = \frac{1}{2\pi\sigma^2\gamma} \, e^{-[(x'/\gamma)^2 + y^2]/2\sigma^2} \quad , \tag{32}$$

where the constant γ expresses the extra uncertainty in the x angle, and is given for some values of θ/σ in Table 3.

Table 3. Values of the parameter γ in equation (32).

θ/σ	γ
0	1.00
1	1.04
2	1.17
3	1.38
4	1.6

The constant-probability contour containing 1/2 of the total probability of the photon direction is an ellipse centered on the track bisector, with semi-major axis 1.176 $\gamma\sigma$ in the plane of the tracks, and semiminor axis 1.176 σ.

While the standard deviation of the gamma-ray direction may be calculated as a function of photon energy, it is convenient to use the measured opening angle of the electron pair as a measure of the electron scattering, hence a measure, on the average, of the photon direction standard deviation, σ. The problem is to find an average relationship between the pair opening angle and the photon direction error.

Assuming all scattering angles to be much less than one radian but much greater than the kinematic opening angles in the pair-production process, the average opening angle of the pair may be expressed in terms of the standard deviations of the projected track angles. Let (x_i, y_i) be the direction of track i, as measured in two orthogonal projections. The probability distribution for each track has the form

$$p(x_i, y_i) = \frac{1}{2\pi \sigma_i^2} e^{-(x_i^2 + y_i^2)/2\sigma_i^2} \; . \tag{33}$$

The separation between the two tracks, i. e. , the opening angle, θ, is given by

$$\theta^2 = (x_2 - x_1)^2 + (y_2 - y_1)^2 \quad , \tag{34}$$

and the average value of the opening angle is

$$\langle \theta \rangle = \int\int\int\int\limits_{-\infty}^{+\infty} \theta \; p(x_1, \; y_1) \; p(x_2, \; y_2) \; dx_1 \; dy_1 \; dx_2 \; dy_2 \quad . \tag{35}$$

Integration of equation (35) yields the result:

$$\langle \theta \rangle = \sqrt{\frac{\pi \; (\sigma_1^2 + \sigma_2^2)}{2}} \quad . \tag{36}$$

The standard deviation of the gamma-ray direction, σ, for a fixed partition of electron energies, is given by equation (26). Thus,

$$\frac{\langle \theta \rangle}{\sigma} = \sqrt{2\pi} \; f\left(\frac{p_1}{k}\right) \quad , \tag{37}$$

where

$$f\left(\frac{p_1}{k}\right) = \left[\frac{\sigma_1^2 + \sigma_2^2}{2 \; \sigma_{eq}^2}\right]^{1/2} \quad . \tag{38}$$

Finally, since the energy division is not known, we need the average value of $f(p_1/k)$ over the allowed range of p_1, for a given photon energy. The average value of f is a slowly varying function of photon energy, which has been computed approximately by numerical integration (Figure 23). As indicated by Olsen (1963), the actual value of θ will have a large spread in individual cases at a given energy. In fact, θ is within a factor of 2 of $\langle \theta \rangle$ for

only about 50% of all events. Thus equation (37) is accurate only for a large number of events. It is a reasonable approximation to take as a constant value for $\langle f \rangle$ its value at a photon energy of 100 MeV (near the peak of the differential photon spectrum), which is approximately 1.6. Then for higher energies, σ will be slightly overestimated, relative to θ. The resulting relationship is
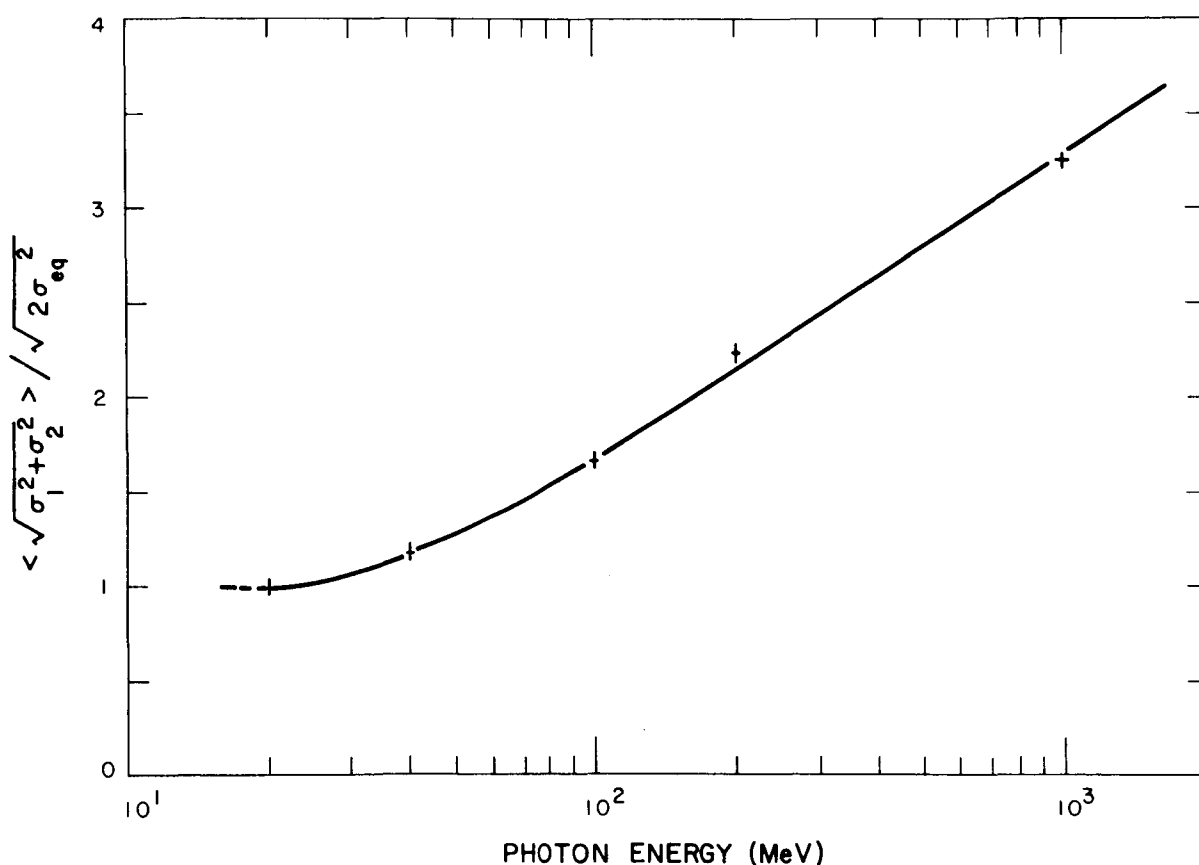
$$\sigma \approx \frac{\langle \theta \rangle}{4} \quad . \tag{39}$$

Figure 23. Ratio of average total standard deviation of track angles, $\langle \sqrt{\sigma_1^2 + \sigma_2^2} \rangle$, to that for equipartition electrons. Points shown were obtained by numerical integration.

The ellipses of constant probability for the direction of the photon relative to the detector then have a major axis to minor axis ratio of approximately 1.6. If the standard deviation in the orientation of the detector (navigation error) is taken as Δ, then in celestial coordinates, the contours containing 50% total probability for the photon direction are approximately ellipses with semimajor axis

$$a = 1.176 \left[\sqrt{(1.3\sigma)^2 + \Delta^2} + 0.3\sigma \right] \tag{40a}$$

and semiminor axis

$$b = 1.176 \left[\sqrt{(1.3\sigma)^2 + \Delta^2} - 0.3\sigma \right] . \tag{40b}$$

For this experiment, the value of Δ is less than or equal to $2°$. Another simplifying approximation is to replace the elliptical cone of resolution just described with a circular cone of the same solid angle. Its half-angle is then

$$c = 1.176 \sqrt{1.6\sigma^2 + \Delta^2} . \tag{41}$$

Figure 24 shows σ, c, and $\langle \theta \rangle$ (inferred from the calculated σ) as functions of photon energy. In Figure 25 are seen the typical opening angles, elliptical contours of 50% total probability, and the circle approximations, both including navigation errors, for several photon energies.
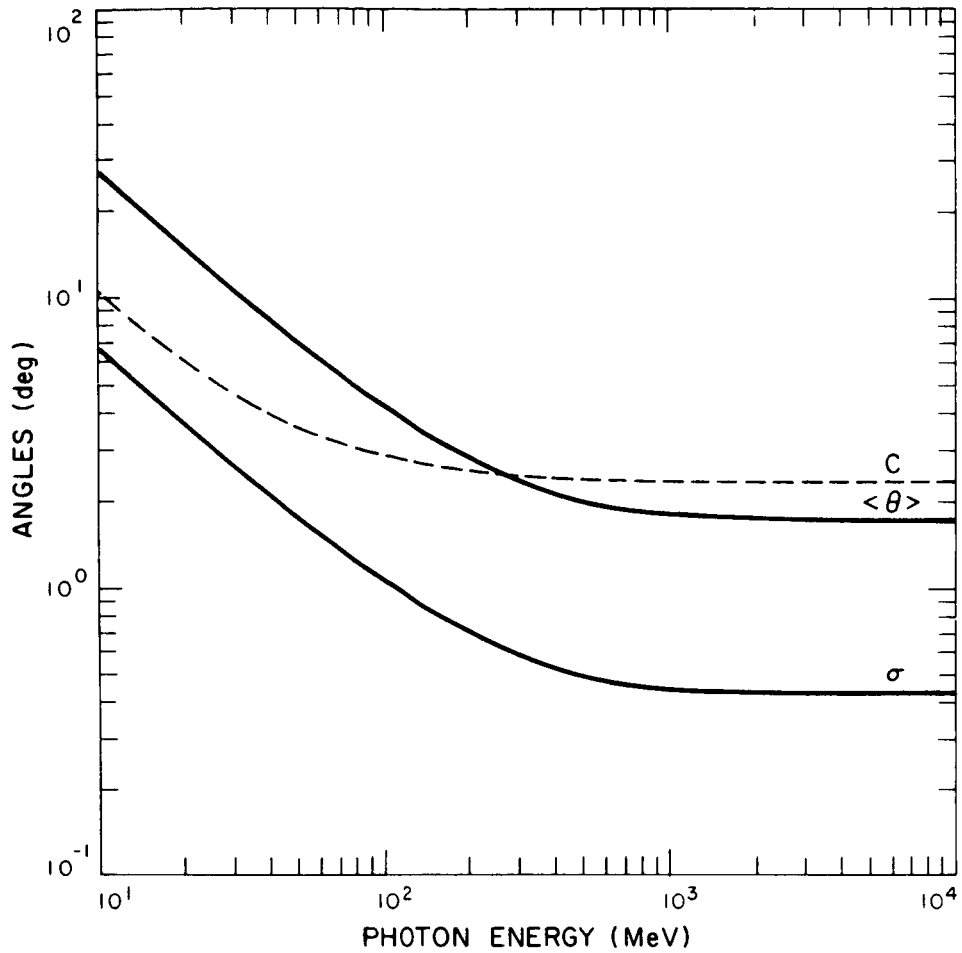
Figure 24. Characteristic angles vs. photon energy (theoretical). Standard deviation of reconstructed photon direction is σ, average opening angle of pairs is $\langle \theta \rangle$, and c is the average resolution cone, assuming a navigation error of $2°$.
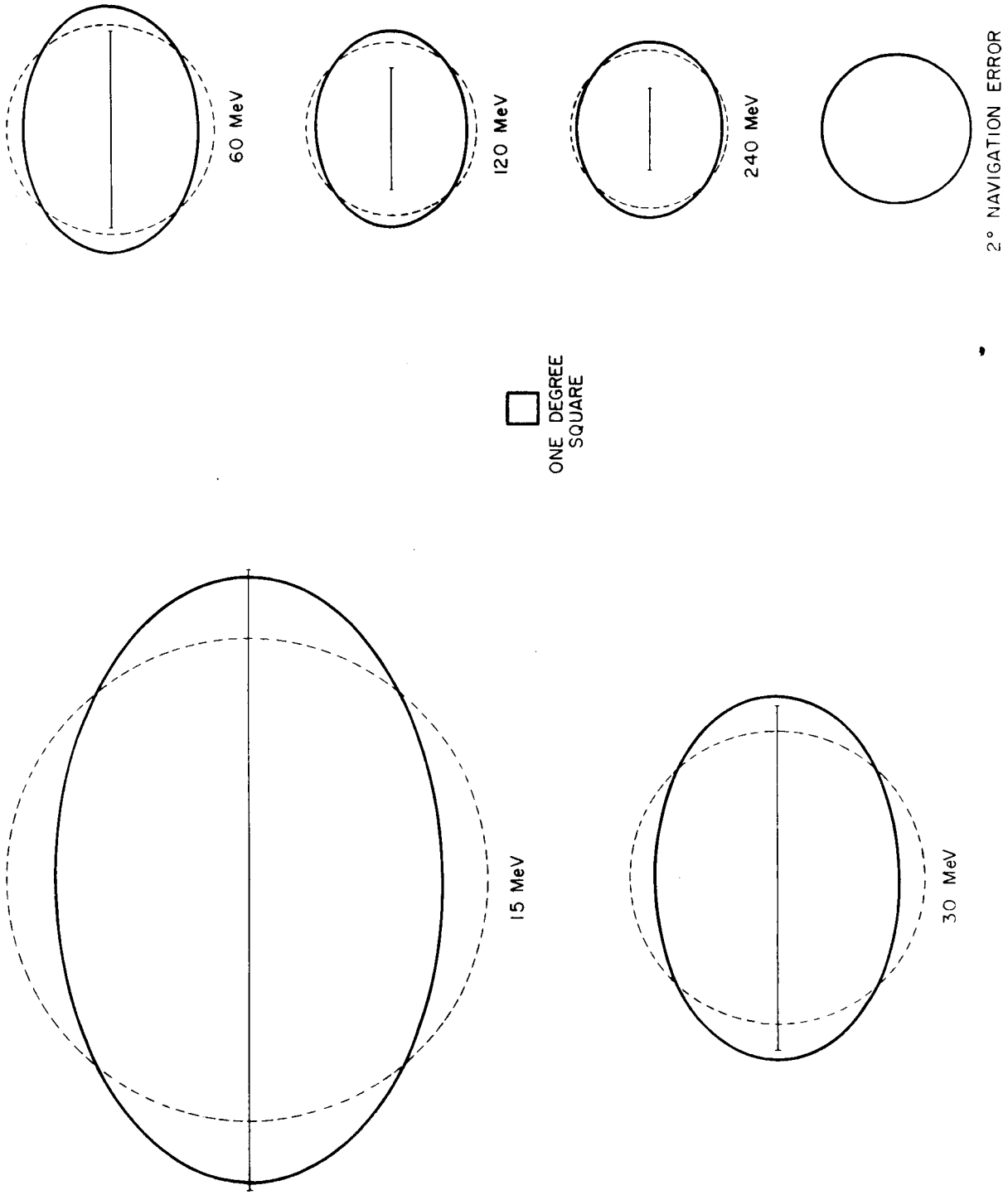
Figure 25. Resolution contours containing 1/2 of source events at indicated photon energies. Straight line: opening angle of electron tracks. Dashed circle: circular cone approximation containing same solid angle. A 2° navigation error is included for all contours.

ACKNOWLEDGMENTS

REFERENCES

CALGARY PROCEEDINGS
  1967.   Proceedings of the Tenth International Conference on Cosmic
          Rays, Calgary, Alberta, Canada (to be published in Can.
          Journ. Phys., May 1968).

DWIGHT, H. B.
  1961.   Tables of Integrals and Other Mathematical Data (4th ed.),
          Macmillan Co., New York, 364 pp. (See p. 323 for normal
          probability integrals.)

EVANS, R. D.
  1955.   The Atomic Nucleus. McGraw-Hill Book Co., New York,
          972 pp.

FAZIO, G. G.
  1967.   Gamma radiation from celestial objects. Ann. Rev. Astron.
          Astrophys., vol. 5, pp. 481-524.

FAZIO, G. G. and HELMKEN, H. F.
  1965.   Vidicon spark chamber system for gamma ray astronomy.
          IEEE Trans. on Nuc. Sci., vol. NS-13, p. 486.

FAZIO, G. G., HELMKEN, H. F., CAVRAK, S. J., and HEARN, D. R.
  1967.   Search for cosmic gamma radiation with a vidicon spark chamber.
          Bull. Amer. Phys. Soc., vol. 12, pp. 582-583. Presented
          at Tenth International Conference on Cosmic Rays, Calgary,
          Alberta, Canada, June 19, 1967 (see CALGARY PROCEEDINGS,
          1967).

HELMKEN, H. F. and FAZIO, G. G.
  1967.   Application of the vidicon spark chamber to gamma-ray
          as ronomy from high-altitude balloons and satellites.
          Presented at Tenth International Conference on Cosmic
          Rays, Calgary, Alberta, Canada, June 19, 1967 (see
          CALGARY PROCEEDINGS, 1967).

HOFSTADTER, R.

    1961. Shower detectors. Methods of Experimental Physics, vol. 5, part A, Nuclear Physics, Ed. by Yuan, L. C. L. and Wu, C. S., Academic Press, New York, pp. 652-668.

ITSA

    1966. Space Disturbances Laboratory Solar-Geophysical Data, June, 1966. Institute for Telecommunication Sciences and Aeronomy, ESSA, Boulder, Colo., Report CRPL-FB-262, 52 pp. (See also Jan., 1966 issue for explanatory notes.)

MATHEWS, J. and WALKER, R. L.

    1964. Mathematical Methods of Physics. W. A. Benjamin, Inc., New York, 475 pp.

OLSEN, H.

    1963. Opening angles of electron-positron pairs. Phys. Rev., vol. 131, No. 1, pp. 406-415.

PENN

    1966. Radio flux record supplied by John P. Hagen, Dept. of Astronomy, Pennsylvania State Univ. (private communication).

PINKAU, K.

    1966a. Molière's theory of multiple scattering applied to the spark chamber. Zeit. f. Physik, vol. 196, pp. 163-173. See also: Erratum. Zeit. f. Physik, vol. 208, p. 418 (1968).

    1966b. The measurement of multiple scattering, of track direction and position in spark chambers. Nuc. Instr. Methods, vol. 48, pp. 173-174.

    1968. Investigation of spark chamber systems with respect to power of resolution in energy, position, and direction. Max-Planck-Institut für Physik and Astrophysik Spec. Rep. MPI/PAE Extraterr. 5/68, Munich, 27 pp.

ROSSI, B.

    1952. High-Energy Particles. Prentiss-Hall, Inc., New York, 569 pp.

WEBBER, W. and CHOTKOWSKI, C. H.

    1967. A charged particle telescope for use in the measurement of the cosmic ray electron spectrum in the energy range 10 MeV-2 GeV. Nuc. Instr. Methods, vol. 49, pp. 45-54.

BIOGRAPHICAL NOTE

DAVID HEARN received the B.S. degree from the California Institute of Technology in 1964 and the M.A. degree in physics from Harvard University in 1966.

He currently holds a Predoctoral Internship from the Smithsonian Research Foundation, and expects to receive his doctorate in physics from Harvard in June 1968.

Mr. Hearn's research interests include elementary particles, cosmic rays, and high-energy astrophysics.